

Reconstructing volcanic radiative forcing since 1990, using a comprehensive emission inventory and spatially resolved sulfur injections from satellite data in a chemistry-climate model

Jennifer Schallock¹, Christoph Brühl¹, Christine Bingen², Michael Höpfner³, Landon Rieger⁴, and Jos Lelieveld¹

¹Atmospheric Chemistry Department, Max Planck Institute for Chemistry, Mainz, Germany

²Royal Belgian Institute for Space Aeronomy, Brussels, Belgium

³Institute of Meteorology and Climate Research, Karlsruhe Institute of Technology, Karlsruhe, Germany

⁴Institute of Space and Atmospheric Studies, University of Saskatchewan, Saskatoon, Canada

Correspondence: Jennifer Schallock (jennifer.schallock@mpic.de)

Abstract.

This paper presents model simulations of stratospheric aerosols with a focus on explosive volcanic eruptions. Using various (occultation and limb-based) satellite instruments, with vertical profiles of sulfur dioxide (SO₂) and vertical profiles of aerosol extinction, we characterized the influence of volcanic aerosols for the period between 1990 and 2019.

5 We established an improved and extended volcanic sulfur emission inventory that includes more than 500 explosive volcanic eruptions reaching the upper troposphere and the stratosphere. Each perturbation identified was derived directly from the satellite data and incorporated as a three-dimensional SO₂ plume into a chemistry-climate model. The simultaneous measurements of SO₂ and aerosol extinction by up to four instruments enabled us to develop a reliable method to convert extinction measurements into injected SO₂. In the chemistry climate model, the SO₂ from each individual plume is converted into aerosol
10 particles and their optical properties are determined. Furthermore, the Aerosol Optical Depth (AOD) and the instantaneous radiative forcing on climate are calculated online. Combined with model improvements, the simulations are consistent with the observations of the various satellites.

Slight deviations between the observations and model simulations were found for the large volcanic eruption of Pinatubo in 1991 and cases where simultaneous satellite observations were not unique or too sparse. Weak- and medium-strength volcanic
15 eruptions captured in satellite data and the Smithsonian database typically inject about 10 kt to 50 kt SO₂ directly into the upper troposphere/lower stratosphere (UTLS) region or transport it indirectly via convection and advection. Our results confirm that these relatively smaller eruptions, which occur quite frequently, can nevertheless contribute to the stratospheric aerosol layer and are relevant for the Earth's radiation budget. These eruptions cause a global radiative forcing of the order of -0.1 Wm^{-2} at the tropopause (compared to a background aerosol forcing of about -0.04 Wm^{-2}).

20 1 Introduction

Next to recent historical events in which large fires have become a major source of aerosols up to the tropopause and above it (Kloss et al., 2019), stratospheric aerosol particles are mostly of volcanic origin and consist of a mixture of liquid sulfuric acid (H_2SO_4) and water (H_2O) droplets (Vernier et al., 2011). The typical median diameter of these aerosol particles ranges between 200 nm for the background aerosol and 600 nm for Pinatubo conditions (Wilson et al., 2008). In this study, we incorporated
25 stratospheric aerosol, the sulfur chemistry and the radiative transfer into a comprehensive Chemistry Climate Model (CCM), which we have used to gain a better understanding of the interaction of aerosols with the global climate system, including chemical effects. Much focus is being placed on adequately modelling and understanding the impact of volcanic eruptions and other aerosol sources on the evolution of the stratospheric aerosol burden.

Sulfate and ashes from explosive volcanic eruptions can account for the majority of the aerosol burden in the stratosphere
30 during volcanically active periods and cause strong temporal and spatial variations in the concentration and the size distribution of the particles (Vernier et al., 2011). These changes influence in turn the radiative forcing at tropopause altitudes (or at the top of the atmosphere) for several years after strong eruptions (Timmreck, 2012) and can even have a more prolonged impact on the global climate (McGregor et al., 2015). After such a volcanic eruption, the enhanced radiative heating exerts an effect on dynamics, influences the global spread of the volcanic cloud and leads to an upward transport of the aerosol itself as well as
35 of other chemical tracers including ozone (Timmreck et al., 1999). The aerosol radiative heating resulting from large volcanic eruptions like Pinatubo triggers enhanced tropical upwelling, which causes a lofting of the injected SO_2 (sulfur dioxide) and the aerosol as well as other chemical tracers. The radiative feedback on dynamics is required to model aerosol extinction in the upper part of the volcanic aerosol plume that corresponds with observations.

Due to the large variability in volcanic emissions, it is challenging to estimate future trends for stratospheric optical depth
40 and forcing (Swindles et al., 2018; Fasullo et al., 2017; Aubry et al., 2021). Therefore, the influence of volcanic eruptions is not included in predictive simulations for future climate scenarios in the IPCC report from 2013 (IPCC, 2013). Previous studies show that model simulations often cannot completely reproduce the AOD of satellite observations or the global forcing of the stratospheric aerosol layer (Solomon et al., 2011), because the number of volcanic eruptions reaching the stratosphere is underestimated in most analyses (Mills et al., 2016; Brühl et al., 2015; Schmidt et al., 2018; Andersson et al., 2015). Conversely,
45 the intensity of single eruptions is sometimes overestimated because of incorrect vertical distribution of the injection patterns in the models. Smaller volcanic eruptions have often been underestimated in previous studies, even though they can be responsible for a radiative forcing that is twice as strong as the background conditions in volcanically quiescent periods such as from 1999 to 2002 (IPCC, 2013; Solomon et al., 2011; Vernier et al., 2011). Friberg et al. (2018) included the whole time series of CALIOP (Cloud-Aerosol Lidar with Orthogonal Polarization) data from 2006 to 2015 and derived stratospheric AOD using
50 reanalysis data for the tropopause, but mentions only medium size eruptions explicitly. Radiative forcing is estimated there from multiplying AOD with -25, an approach which is valid only for purely scattering aerosol. GLOSSAC (Thomason et al., 2018; Kovilakam et al., 2020), a time dependent aerosol climatology sometimes used for climate simulations, has a coarse temporal resolution, many discontinuities in space and time due to change of instruments or measurement gaps and excludes

important satellite data (e.g. MIPAS). It does not provide SO₂ needed as input for chemistry climate models directly but
55 only extinction and indirectly derived quantities like estimates of aerosol surface area density and mode radius assuming
unrealistic monomodal size distributions. We therefore prefer to recalculate SO₂ injections into the stratosphere based on the
Smithsonian volcano database and the most recent releases of satellite data sets, in particularly those gathered using limb
sounding instruments to derive information on the vertical distribution.

For the ENVISAT (European Environmental Satellite) period 2002-2012 a first version of a new volcanic SO₂ inventory
60 with improved temporal and spatial resolution was developed within the framework of ISA-MIP (Timmreck et al., 2018; Brühl
et al., 2018). The corresponding data base (https://doi.org/10.1594/WDCC/SSIRC_1) contains 3D-SO₂-perturbations derived
from satellite data as well as integrated injected SO₂ masses. In this work the data base is expanded to the period 1990-2019
and considerably improved for the period 1998-2001. The simultaneous measurements from up to four instruments from 2002
to 2011 enabled us to develop a novel procedure for conversion of aerosol extinction to SO₂ needed for the period before and
65 after ENVISAT.

Our method circumvents problems and uncertainties related to the classical point source approach like dependence on the
box size and location, the time interval during which the mass is injected, and effects of microphysical and chemical interactions
of SO₂ and sulfate with injected volcanic ash and water in the early phase (Zhu et al., 2020).

Non-eruptive permanently degassing volcanoes represent another natural source of aerosols, which are treated separately
70 from active explosive volcanic eruptions. For the stratosphere these contribute in most cases only to the background since most
of the released SO₂ is removed by oxidation and rainout in the troposphere. This holds also for the medium size eruption of
Eyjafjallajökull in 2010 from which almost no SO₂ reached the stratosphere as shown by MIPAS observations. Stratospheric
H₂SO₄ is also produced from non-volcanic sulfur precursor gases, like carbonyl sulfide (OCS) (Crutzen, 1976), dimethyl
sulfide (DMS) (Kettle and Andreae, 2000), and tropospheric SO₂ from pollution, which constitute a source of background
75 concentration of stratospheric aerosol. To improve the accuracy of the sulfur budget of the stratosphere in the CCM, sources
and sinks of sulfur as well as its precursor gas components have to be identified.

This paper is structured as follows: section 2 presents satellite data used for entering the volcanic perturbations of aerosols
and SO₂ into the model, and for model evaluation. In section 3, the setup used for the climate model simulations is described.
Section 4 contains a volcanic sulfur emission inventory with all relevant explosive volcanic eruptions detected between 1990
80 and 2019, which are included in the model simulations in section 5. The influence of these volcanic eruptions on the stratosphere
and climate is analysed in section 6. At the end of section 6 as well as in the final discussion (section 7), the results are discussed
in a wider context.

2 Satellite observations

To generate the input data from volcanic eruptions for our simulations, we analysed satellite data sets from two instruments on
85 the European Environmental Satellite (ENVISAT) that was launched on 1 March 2002 and lost signal on 8 April 2012, namely
MIPAS and GOMOS. Furthermore, the OSIRIS instrument on board the Odin satellite was used to provide additional data

for the period up to 2019. For the period before 2002, we used the SAGE II instrument. The data processing is described in section 4. Some examples for eruptions where simultaneous observations from all these instruments or at least 3 were available for cross validation are presented in the Appendix B.

90 2.1 Michelson Interferometer for Passive Atmospheric Sounding (MIPAS)

MIPAS was a mid-infrared emission spectrometer on board the ENVISAT satellite. MIPAS scanned the limb, thereby analysing the infrared radiation emitted by the Earth's atmosphere at different tangent altitudes (Fischer et al., 2008).

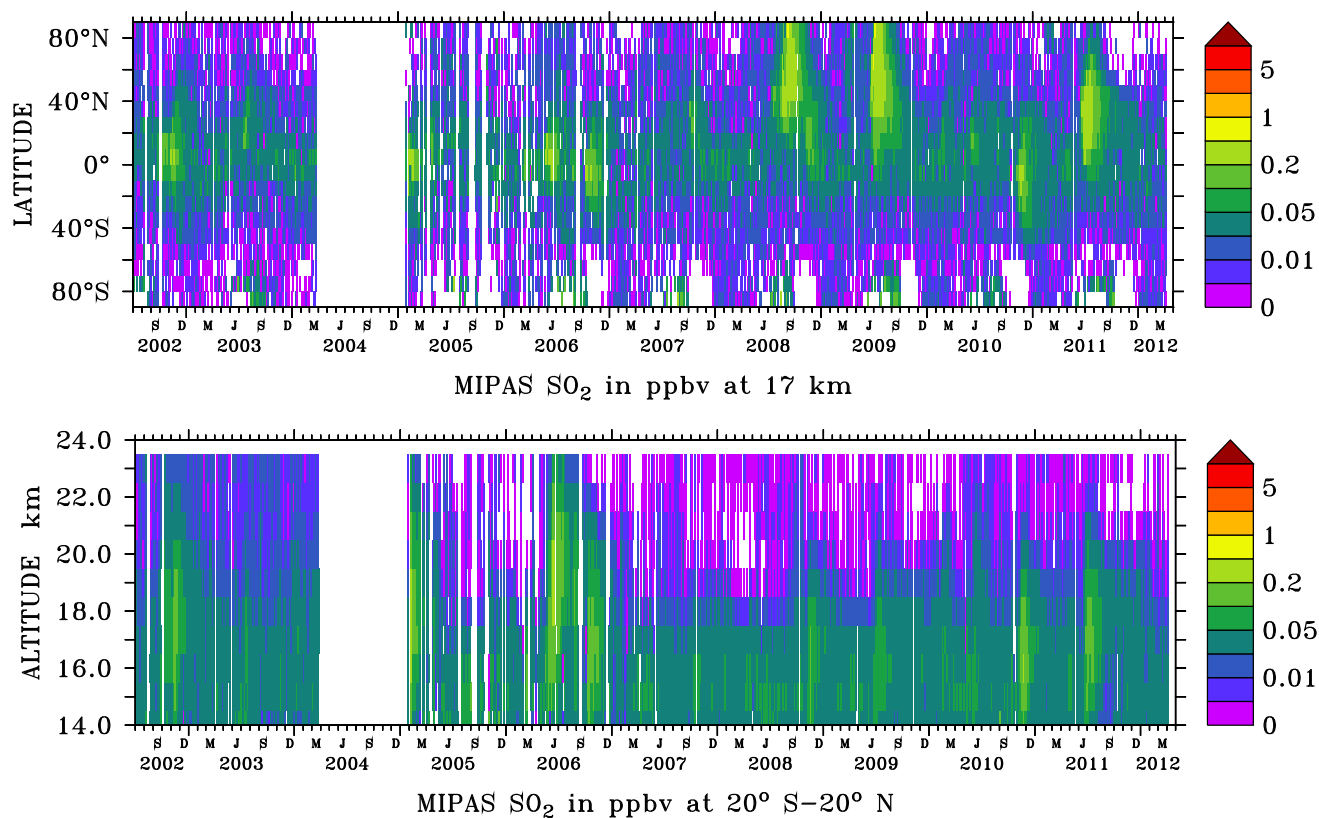


Figure 1. The volume mixing ratios of SO₂ in ppbv as derived from the MIPAS instrument (Höpfner et al., 2015). The dataset spans the period 1 July 2002–8 April 2012: Horizontal distribution at 17 km altitude (top) and vertical distribution for tropical regions 20° S–20° N (bottom). White: no data.

The atmospheric spectra ranging from 4.15 μm to 14.6 μm are inverted to provide vertical profiles of temperature and volume mixing ratios of more than 25 different trace species, like the sulfate aerosol precursor gases SO₂ and OCS (Glatthor et al., 2015, 2017; Höpfner et al., 2013, 2015), as well as H₂O, ozone (O₃), methane (CH₄), nitrous oxide (N₂O), nitrogen dioxide (NO₂) and nitric acid (HNO₃), among others.

Vertical SO₂ profiles (Figure 1) from the MIPAS SO₂ single profile retrieval (Höpfner et al., 2015) were used to identify plumes of volcanic eruptions. We utilised a gridded dataset from these retrievals with a three-dimensional sampling of 60° longitude, 10° latitude, 1 km altitude with a vertical coverage of 10 km to 23 km and a temporal averaging of five days. The lower altitude limit varies with the tops of clouds in the troposphere, especially in tropical regions.

The typical estimated random uncertainty for a single measurement of a volume mixing ratio profile is estimated to be 70–100 pptv. For the gridded dataset used here, systematic uncertainties are more important. These were estimated to be 10–75 pptv (10–180 %) under background concentrations and 10–110 pptv (10–75 %) under volcanic influence (Höpfner et al., 2015).

2.2 Global Ozone Monitoring by Occultation of Stars (GOMOS)

The Global Ozone Monitoring by Occultation of Stars (GOMOS) instrument on ENVISAT operates based on the principle of stellar occultation. GOMOS provides data on stratospheric aerosol extinction as well as O₃, NO₂, nitrogen trioxide (NO₃) and air density (Kyrölä et al., 2010). The principle of stellar occultation is described in detail in Bertaux et al. (2010). In short, this self-calibrating sounding method scans the atmosphere by pointing to a star during its sunset or sunrise. The measured spectra vary with the tangent altitude due to the absorption and scattering of light by the different atmospheric species along the line of sight.

In a first step, the GOMOS inversion algorithm determines the slant column density of gaseous species and the slant aerosol optical depth along the optical path (Vanhellemont et al., 2004). This process makes use of reference absorption spectra of the main absorbing species (such as the ones provided by the MPI-Mainz UV/VIS Spectral Atlas of Gaseous Molecules of Atmospheric Interest (http://satellite.mpic.de/spectral_atlas) and extinction cross-section values representative for aerosols. In a second step, vertical density profiles of the target gas species and vertical profiles of the aerosol extinction coefficient are obtained from the slant quantities (Bertaux et al., 2010).

GOMOS uses four spectrometers providing measurements at wavelengths from the UV-visible to the near-IR range in four spectral regions: 248 nm–371 nm, 387 nm–693 nm, 750 nm–776 nm, and 915 nm–956 nm (Robert et al., 2016). As the original inversion algorithm (the operational algorithm IPF) was poorly effective for the retrieval of the aerosol extinction coefficient and only one extinction channel was obtained at the reference wavelength of 550 nm (Vanhellemont et al., 2010), a new retrieval algorithm called AerGOM was designed (Vanhellemont et al., 2016; Robert et al., 2016) in order to improve the spectral inversion. Also, the cross-section spectra were revised using up-to-date reference spectra (Bingen et al., 2019). AerGOM provides the spectral dependence of the aerosol extinction coefficient between about 350 nm and 750 nm.

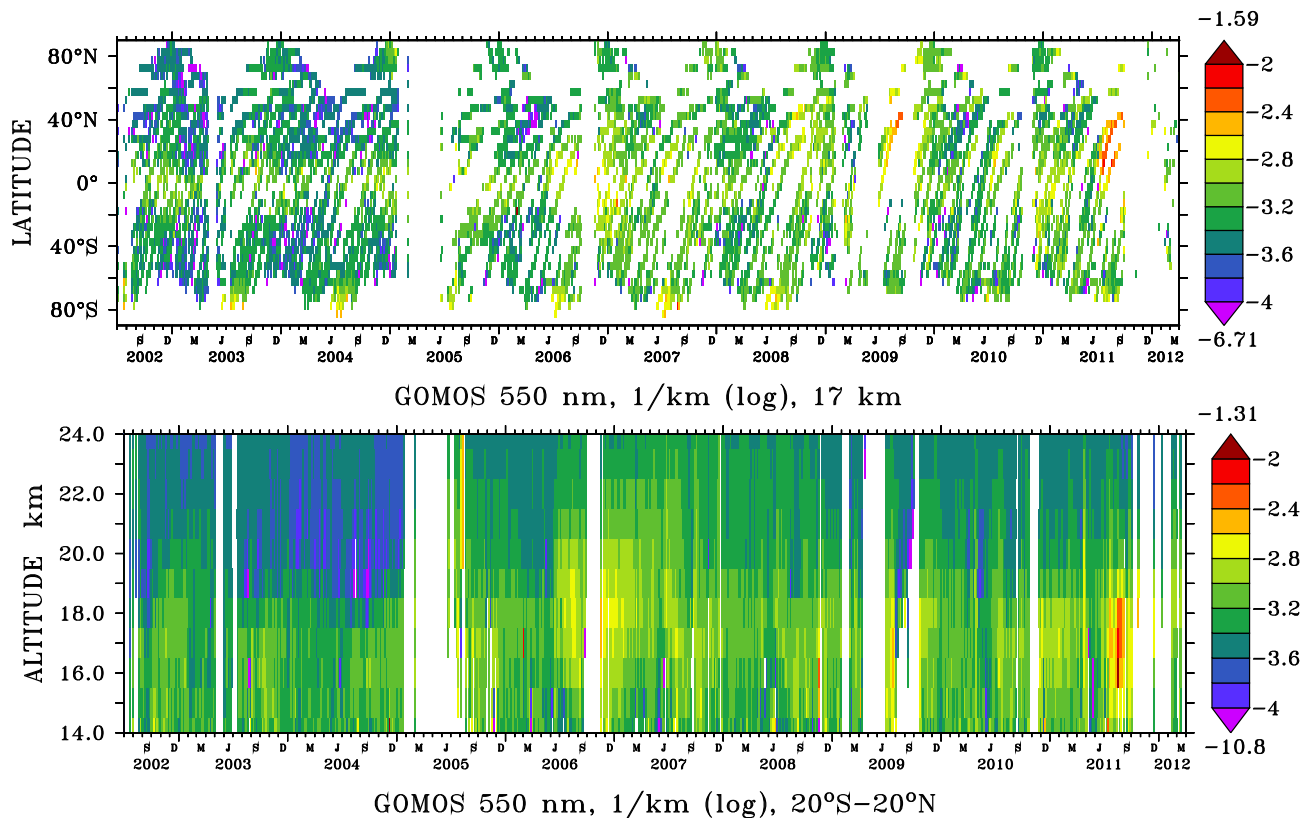


Figure 2. The decadal logarithm (log) of the aerosol extinction coefficient (1/km) as derived from the GOMOS instrument data v.3.00 at **550 nm wavelength** from Bingen et al. (2017). The dataset spans the period 15 April 2002–8 April 2012: Horizontal distribution at 17 km altitude (top) and vertical distribution for tropical regions 20° S–20° N (bottom). Maximum and minimum values appear above (dark red) and below (violet) the colour keys, respectively. White: no data.

The typical extinction uncertainty exhibits large variability in function of the star parameters (from about 5–15 % in the most favourable cases of bright, hot stars, to about 40–70 % in the less favourable cases of dim, cold stars) (Bingen et al., 2017). A full validation of AerGOM, version 1.0, is presented by Vanhellefont et al. (2016). A main factor influencing the uncertainty is the weakness of the star signal, which is alleviated by the high measurement rate made possible by the abundance of stars. The large variability in magnitude and temperature of the occultated stars also significantly influences the measurement uncertainty (Robert et al., 2016).

From AerGOM, climate data records were processed for use in chemistry-climate models (Bingen et al., 2017), and these are the data sets used in the present study. Figure 2 and Figure 3 show the aerosol extinction from the GOMOS instrument at wavelengths of 550 nm (Figure 2) and 750 nm (Figure 3), respectively. In both cases, a gridded aerosol extinction dataset is used (CCI-GOMOS dataset in version 3.00, see Bingen et al. (2017)).

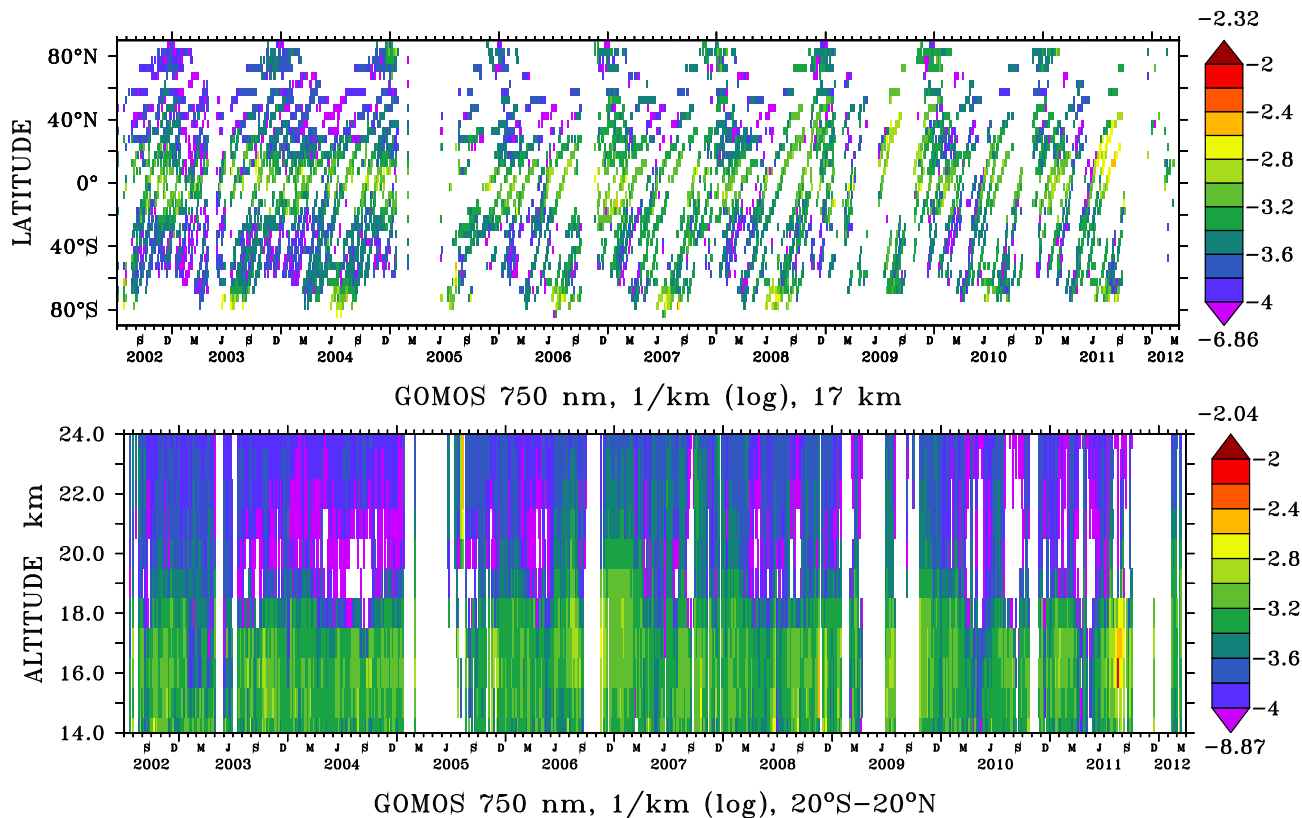


Figure 3. The decadal logarithm (log) of the aerosol extinction coefficient (1/km) as derived from the GOMOS instrument data v.3.00 at **750 nm wavelength** from Bingen et al. (2017). The dataset spans the period 15 April 2002–8 April 2012: Horizontal distribution at 17 km altitude (top) and vertical distribution for tropical regions 20° S–20° N (bottom). Maximum and minimum values appear above (dark red) and below (violet) the colour keys, respectively. White: no data.

The resolution of the CCI-GOMOS dataset was optimized to a grid of 5° latitude by 60° longitude and a time resolution of five days. This choice is made possible by the high measurement rate and is more suitable for describing the aerosol distribution than zonal monthly means, because it allows detection of the signature of aerosol patterns with a lifetime of as short as a week (e.g., medium-sized volcanic eruptions).

2.3 Optical Spectrograph and InfraRed Imaging System (OSIRIS)

The dataset from the Optical Spectrograph and InfraRed Imaging System (OSIRIS) allowed us to extend the time series beyond April 2012, after which the signal of the ENVISAT satellite was lost. OSIRIS is a limb scatter instrument, which was launched on board the Odin satellite on 20 February 2001 and is still operating today.

OSIRIS performs limb scans of atmospheric radiance spectra at wavelengths from the UV to the near-IR ranges (274 nm–810 nm) (Bourassa et al., 2012). To obtain the vertical profiles of aerosol extinction at altitudes from 10 km to 35 km (Rieger

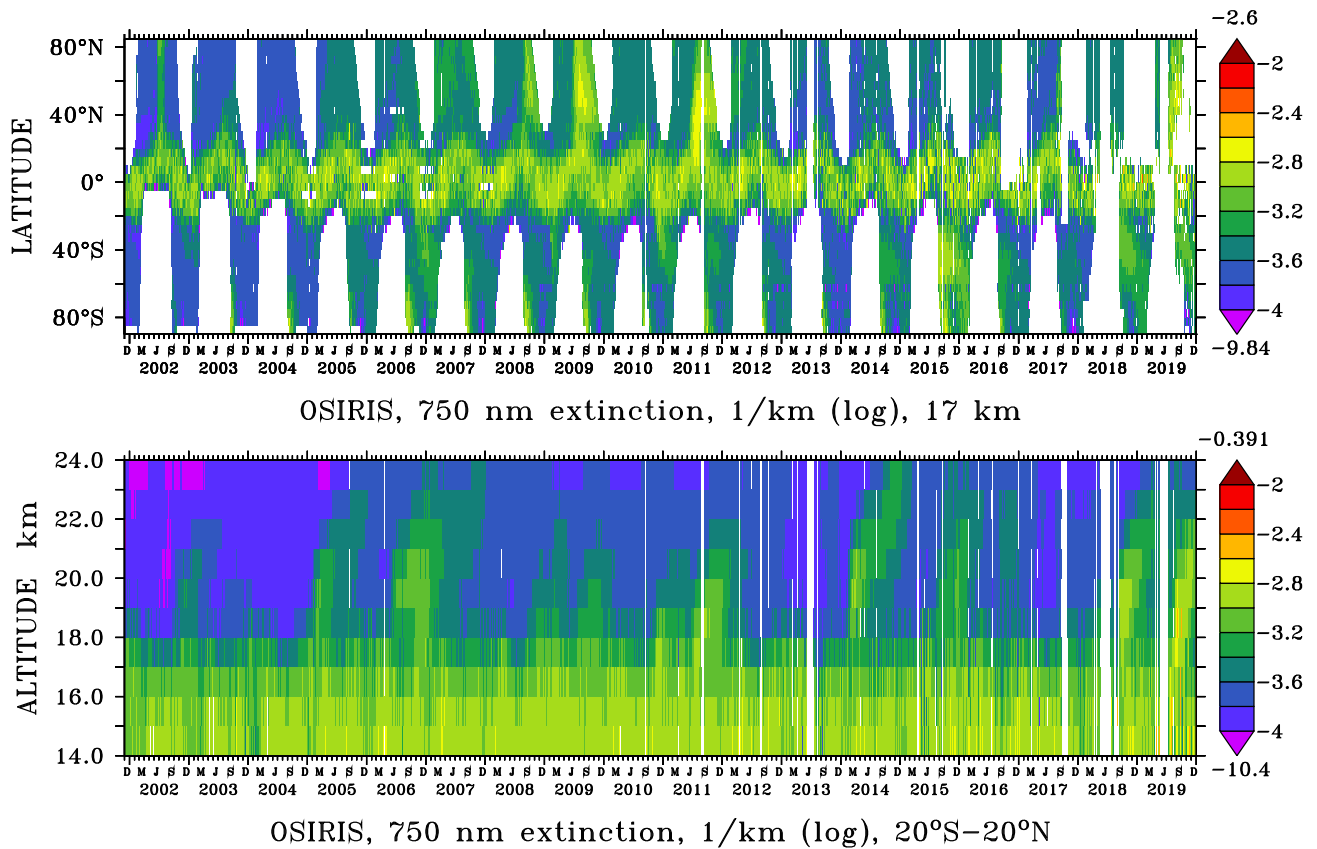


Figure 4. The logarithm $\log(1/\text{km})$ of the aerosol extinction as derived from the OSIRIS instrument at **750 nm wavelength** by Bourassa et al. (2012) and Rieger et al. (2019). The dataset spans the period 1 July 2002–December 2019: Horizontal distribution at 16.5 km altitude (top) and vertical distribution for tropical regions 20° S–20° N (bottom). Maximum and minimum values appear above (dark red) and below (violet) the colour keys, respectively. White: no data.

et al., 2015), the aerosol scattering properties are calculated with a refractive index of $1.427 + i7.167 \times 10^{-8}$ using Mie theory at
 145 750 nm wavelength and a sulfate concentration of 75 % H_2SO_4 and 25 % H_2O (Rieger et al., 2018).

For this study, the OSIRIS version 5.10 aerosol retrieval was used until October 2017 and the version 7.1a afterwards (for details see Rieger et al. (2019); Bourassa et al. (2012)). OSIRIS provides a surface coverage from 82° S–82° N, except in polar winter when there is no sunlight and except in the Southern Hemisphere winter when tangent point is not illuminated by the sun (see Figure 4). The vertical grid resolution is 1 km altitude, 5° latitude and 30° longitude with 5-day-averaged time intervals.

150 The total uncertainty is about 10–15 % in the aerosol layer between 15–30 km, where the sensitivity of the measurements decreases with increasing optical depth. Due to measurement noise, the uncertainty dominates the signal above 30 km and in the troposphere (Rieger et al., 2015). At altitudes near and below the tropopause, the OSIRIS measurements are sensitive to

clouds that may be interpreted as elevated aerosols. This is likely contributing to larger background extinction values measured below approximately 17 km in the tropics, as can be seen in Figure 4 (bottom), and the uncertainty is higher.

155 2.4 Stratospheric Aerosol and Gas Experiment II (SAGE II)

SAGE II was a solar occultation instrument that performed measurements during sunrise and sunset. The SAGE II aerosol extinction measurements on board the Earth Radiation Budget Satellite (ERBS) started in October 1984 and ended in August 2005. This data set is important for the model setup before the ENVISAT period starting in 2002. The aerosol extinction gridded using 60° longitude and 10° latitude intervals is derived from the V7.00 L2 profiles provided by the Earth Observing
 160 System Data and Information System of NASA (EOSDIS) database (Figure 5).

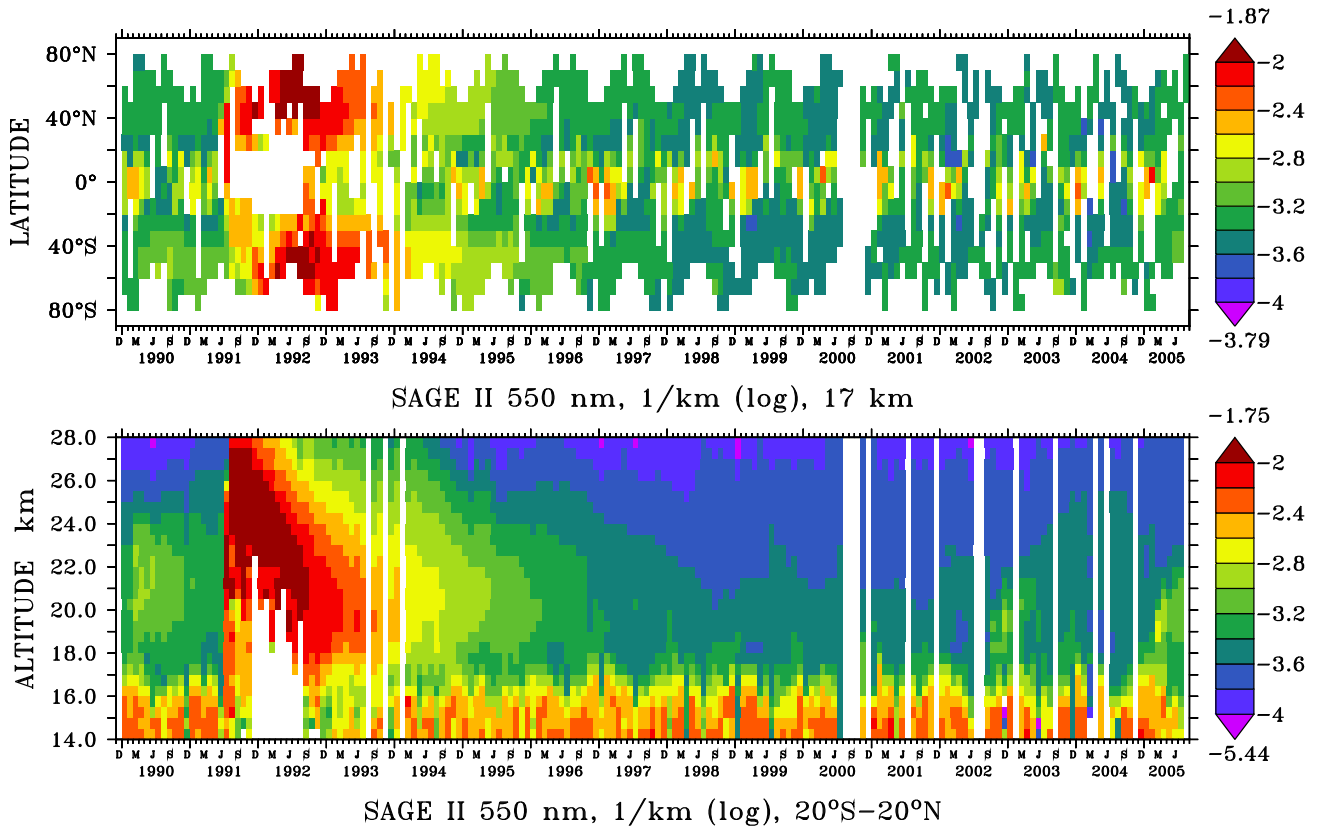


Figure 5. The logarithm of the extinction coefficient (1/km) of the SAGE II instrument from Thomason et al. (2008). The dataset spans the period January 1990–August 2005: Horizontal distribution at 16.75 km altitude (top) and vertical distribution for tropical regions 20° S– 20° N (bottom). Maximum and minimum values appear above (dark red) and below (violet) the colour keys, respectively. White: no data.

The gridded SAGE II dataset used in the present study provides a near-global coverage with latitudes between 80° N to 80° S, with a horizontal grid resolution of 60° in longitude, 10° in latitude and a vertical resolution of 0.5 km between 13 km

and 30 km altitude. SAGE II measured in occultation, thus, its measuring principle is similar to that of GOMOS. The two main differences between GOMOS and SAGE II, are that the latter used the sun as light source, which results in a much better signal-to-noise ratio. On the other hand, its measurement rate is much lower than that of GOMOS, since only two measurements (one sunrise and one sunset) are possible per orbit, so that a near-global coverage is achieved in about one month.

Measurements occur at seven wavelengths between 386 nm and 1020 nm. The vertical profiles of O₃, NO₂ and water vapor are provided as well as aerosol extinction coefficients at four wavelengths (386, 452, 525 and 1020 nm) from the middle troposphere to the upper stratosphere.

After the large eruption of Mount Pinatubo in 1991, “saturation” effects at lower altitudes were observed in the profiles for more than one year, meaning that the aerosol load was so high that the light signal received by the instrument was below the limit of detection. This effect corresponds to the large white areas for 1991 and 1992 in Figure 5. Red pixels around 14–16 km correspond to measurements contaminated by clouds, increasing the optical depth in the upper troposphere/lower stratosphere (UTLS) region on the lower panel of Figure 5. The perturbations by convective clouds occur mostly over the West Pacific and were excluded in the procedure for estimating the SO₂ injections. The data gaps in the year 2000 were caused by an instrument failure causing SAGE II to be switched off for several months.

The uncertainty of the operational SAD (surface area density) product during background periods is affected by several parameters, including the lack of sensitivity to particles with radii smaller than 100 nm, the number of degrees of freedom indicated by the averaging kernels of the aerosol extinction at different wavelength channels and the temperature profile used in the data processing (Thomason et al., 2008). SAD is used in GLOSSAC.

3 Description of the setup for the EMAC Model

The model simulations performed in the period from 2002 to 2012 by the global atmospheric chemistry climate model EMAC in Bingen et al. (2017) and Brühl et al. (2018) were extended to 1990 to 2019 in this study. For these model simulations, a higher horizontal resolution T63 (1.87° × 1.87°), instead of T42 (2.81° × 2.81°) in Bingen et al. (2017), was chosen. As we here focus on the stratosphere, the middle atmosphere version L90 with 90 layers up to 0.01 hPa (~80 km) and high vertical resolution in the lower stratosphere was needed (Giorgetta et al., 2006). The dynamical model is nudged to the meteorological ERA-Interim reanalysis data of the European Centre for Medium-Range Weather Forecasts (ECMWF) up to about 100 hPa.

As EMAC is a very complex chemistry climate model it contains many submodels and functions which are essential for running the simulations but are not directly related to the sulfur cycle, these are mentioned in Appendix A. In this section we focus on the sulfur cycle.

The plumes of outgassing volcanic SO₂ emissions (Diehl et al., 2012) are imported via the OFFEMIS submodel as 3-D field volume emission fluxes (Kerkweg et al., 2006b). The exchange of dimethyl sulfide (DMS) between the air-sea interface of the ocean and the atmosphere is simulated by the AIRSEA submodel (Pozzer et al., 2006).

The gas- and aqueous-phase chemistry in the troposphere and stratosphere is calculated interactively with the CAABA/MECCA (Chemistry As A Boxmodel Application/Module Efficiently Calculating the Chemistry of the Atmosphere) submodel (Sander

et al., 2011). Specifically, the chemically generated SO_2 is calculated from fluxes of sulfate precursor gases and further transformed to H_2SO_4 (Brühl et al., 2018), together with the emitted SO_2 . OH and ozone are fully interactive. CAABA/MECCA is also coupled to the Multiphase Stratospheric Box Model (MSBM) for heterogeneous reactions on aerosols and Polar Stratospheric Clouds (PSCs) (Jöckel et al., 2010) to allow for feedback on ozone. Calculated sulfate is used by MSBM for heterogeneous chemistry. The uptake and oxidation of tracers is considered by the SCAVenging submodel for both liquid and mixed phase clouds (Tost et al., 2006a), also including the aqueous sulfur oxidation of SO_2 to SO_4^{2-} .

For parametrisation of aerosol microphysical processes, we used the Global Modal-aerosol eXtension (GMXe) aerosol module (Kerkweg, 2005; Stier et al., 2005; Vignati et al., 2004) and we described aerosol species using four soluble and three insoluble interacting lognormal aerosol modes. The original mode boundaries of the aerosol size distribution from Pringle et al. (2010) were adapted for this setup to volcanic aerosol conditions in the stratosphere as shown in Table 1 to avoid overly rapid sedimentation of coarse aerosol particles after big volcanic eruptions. The nucleation of new particles consists only of completely soluble sulfate aerosols and is calculated by the parametrisation used by Vehkamäki et al. (2002). Further, the evaporation of liquid sulfate particles back to the gas phase in the middle stratosphere is possible in the model.

Mode boundaries	Pringle et al. (2010)	σ	Brühl et al. (2018)	σ
Nucleation mode: soluble	<10 nm	1.69	1 nm–12 nm	1.59
Aitken modes: soluble & insoluble	10 nm–100 nm	1.69	12 nm–140 nm	1.59
Accumulation modes: soluble & insoluble	100 nm–1 μm	1.69	140 nm–3.2 μm	1.49
Coarse modes: soluble & insoluble	>1 μm	2.2	>3.2 μm	1.7

Table 1. Diameters of aerosol mode boundaries in the GMXe submodel for tropospheric (Pringle et al., 2010) and volcanic stratosphere conditions (Brühl et al., 2018), including the corresponding mode distribution width (σ).

The AERosol OPTical properties in the model are calculated online with the AEROPT submodel (Dietmüller et al., 2016) and are coupled to the GMXe submodel. The resulting extinction coefficient is given at wavelengths of 350, 550, 750 and 1025 nm for comparison with GOMOS, OSIRIS and SAGE. Finally, the aerosol optical properties like wavelength-dependent particle extinction cross section, single scattering albedo, and asymmetry parameter for each aerosol mode from AEROPT (Dietmüller et al., 2016) are used in the radiation scheme as input for the radiative transfer calculations and to calculate the AOD. The influence of stratospheric aerosol on instantaneous radiative forcing and heating is calculated online for diagnostic purposes (for details see Dietmüller et al. (2016)). Via multiple calls of the RAD submodel, the instantaneous forcing is simulated with stratospheric aerosol above 100 hPa only and without any aerosol (Brühl et al., 2012). The lowermost level of the RAD_FUBRAD sub-submodel for the upper atmosphere is shifted from above 70 hPa in the original version of Dietmüller et al. (2016) to 30 hPa–14 hPa to allow for scattering by the aerosol in the simulations with volcanic emissions.

4 Volcanic Sulfur Emission Inventory

220 In a previous inventory of volcanic eruptions based on SO₂ vertical profiles from MIPAS, we estimated the aerosol radiative forcing from 2002 to 2011 by simulating the evolution of SO₂ in the atmosphere reported by Brühl et al. (2015) and by improving the resulting time series using aerosol measurements from Bingen et al. (2017). The results of these simulations showed that significant discrepancies remained with respect to radiative forcing estimated from measurements (Brühl et al., 2018).

225 In this work, we further improve the volcanic sulfur emission inventory by analysing additional satellite data sets (section 2) and by including all identified relevant eruptions between 1990 and 2019. To derive the volcanic 3D SO₂ perturbation from MIPAS we normally select the five day interval at the time of the eruption and the following one. For medium size eruptions up to 6 consecutive intervals are used to correct for saturation effects or artefacts from the applied cloud clearing scheme in case of ash (Höpfner et al., 2015). As background about 10 pptv, the typical value originating from OCS oxidation, is subtracted. In
230 some cases this value can be larger because of remnants of a previous volcanic event.

The amount of sulfur emitted by each single eruption is calculated by integration of SO₂ vertical profiles from MIPAS observations, excluding tropospheric emissions below 12 km at high latitudes, 13 km at mid-latitudes, and 14 km at low latitudes to include possible convective transport from the upper troposphere into the stratosphere in the tropics. The limits in mid and high latitudes above the mean tropopause were selected to exclude cloud perturbations by frontal systems. These limits hold
235 also for the SO₂ estimates from the other instruments.

The GOMOS dataset is very important to compensate for data missing from the MIPAS instrument (subsection 2.1), where several important eruptions in 2004 and 2006 could not be identified (Bingen et al., 2017). An appropriate comparison of SO₂ mixing ratio measurements from MIPAS and of the aerosol extinction from GOMOS requires consideration of a time shift of one to two weeks as a result of the particle formation from the gas phase. We typically select a 10-day period beginning
240 about a week after the eruption. Then the SO₂ mixing ratio perturbation is derived from the extinction by using a ratio between model calculated sulfate volume mixing ratio and its share on extinction in the lower stratosphere of low latitudes, dividing by air density, and subtracting a typical background (see Appendix B). We assume that the spatial patterns of the perturbation of extinction and sulfate are the same as for SO₂. A similar technique is used for OSIRIS and can be used for SAGE II data.

If data gaps cause a shift of the time period away from the maximum perturbation or a bias in the zonal average, a correction
245 factor is applied, which can be as high as 3 if the shift is three months as for Calbuco. To estimate the factor, we iterated calculated extinctions to agree with OSIRIS and also used observations and assumptions by Vernier et al. (2016). Correction factors up to 2 have to be applied in some cases because of data gaps, incomplete profiles or for high latitudes (see Appendix B). On the other hand, the factor can be as small as 0.5 to account for remnants of eruptions occurring 2 weeks before or cloud perturbations.

250 For SAGE II in most cases the SO₂ mixing ratio is derived using the parameterisation of Grainger et al. (1995) which converts SAD to volume density as first step. We use pressure and temperature provided to convert from mass density to a

volume mixing ratio, assuming that observed sulfate is produced from injected SO₂ some weeks ago. With this method it is easier to correct for cloud contamination than by using the extinction directly as above for the other instruments.

Case studies for 3 events, comparing SO₂ results from the different satellites and the different conversion methods are presented in Appendix B.

Additional SO₂ column data from the Ozone Monitoring Instrument (OMI), Total Ozone Mapping Spectrometer (TOMS), Ozone Mapping and Profiler Suite (OMPS) (not shown here) and other satellites were also used to verify the consistency of the data and to fill in data gaps, marked as white areas in all satellite images. Especially in 2018 and 2019 the OSIRIS data are so sparse that constraints from instruments like OMPS or analogues events of previous years have to be superimposed for some eruptions.

Geological information and additional observations on plume heights were received from the Global Volcanism Program, Smithsonian Institution (<https://volcano.si.edu/>). Their reports several times indicate that even VEI 2 eruptions (volcanic explosivity index) can reach the upper troposphere (or lower stratosphere which confirms the satellite observations).

The resulting volcanic emission inventory is presented in Table 2 and provides the injection time into the model, the coordinates of the ejected plume and the amount of emitted SO₂. Each volcano is identified by its name if available, or by the concerned region if the name is unknown. The altitudes and latitudes indicated in the table correspond to the locations of the maximum SO₂ mixing ratios of the volcanic plumes. The longitudes refer to the locations of the volcanoes, because the plumes have been moved by the zonal winds during the time lag between eruption and observation. In the cases of OSIRIS, SAGE and GOMOS this shift can easily be 100 degrees.

It should be noted as well that the date of the volcanic eruption can differ by a few days from the date of injection in the model simulation, because the temporal resolution of the data sets is about five days at least (or weeks in the SAGE period). In a lot of cases, more than one eruption is found in the same time step within an interval of five days. In such a case, all eruptions are listed in the same line. Several time the used time period for extraction has to be extended because of data gaps, which increases the uncertainty and complicates the identification of the right volcano. In such a case, the name of the most probable volcano is tagged with a "?". If the SO₂ emissions of two volcanoes cannot be separated with certainty, both are indicated with a "+" in the same line. This uncertainty is frequent in the Republic of Vanuatu, an island country located in one of the most volcanically active regions in the South Pacific, referred to as "Vanuatu" in Table 2.

When comparing the SO₂ emissions reported here with those of Carn et al. (2016), it should be noted that Carn et al. (2016) makes use of total SO₂ emissions, including rapidly removed tropospheric SO₂, while the present study only takes into account the long-lived, climate-relevant stratospheric fraction of the emitted SO₂. A comparison of the injected volcanic SO₂ masses per year is presented in Appendix C.

Volcano or region	Time	Latitude (°)	Longitude (°)	Altitude (km)	SO ₂ (kt)	Instrument
Kelut	11 Feb 1990	-8	112	16, 22	410	S
Gamalama	25 Apr 1990	0	127	16	96	S
Raung (?)	25 Jul 1990	-8	115	16	63	S

Volcano or region	Time	Latitude (°)	Longitude (°)	Altitude (km)	SO ₂ (kt)	Instrument
Pacaya + Sabancaya	16 Sep 1990 6 Oct 1990	15 -16	-90 -72	16 17	10 75	S S
Papua + Fernandina Pinatubo Hudson	12 Jan 1991 20 Apr 1991 16 Jun 1991 10 Aug 1991	-4 0 15 -46	145 -92 120 -73	17 16 23 18	88 118 16942 1276	S S S S
Cerro Negro Spurr Spurr Spurr	10 Apr 1992 28 Jun 1992 19 Aug 1992 18 Sep 1992	12 61 61 61	-87 -152 -152 -152	22 17 16, 18 17	18 291 298 187	S S S S
Lascar Langila, Galeras (?)	18 Apr 1993 30 Oct 1993	-23 -5, 1	-68 145, -70	22 17	376 50	S S
Yasur? Rinjani, Nyamuragira, Central America Rabaul Merapi, Ecuador	17 Mar 1994 6 Jul 1994 20 Sep 1994 23 Nov 1994	-16 -8, -1, 12 -4 -7, 1	165 117, 30, -90 150 110, -70	16 16 18, 22 17, 17	80 63 89 48, 57	S S S S
Peru, Africa, Vanuatu Mexico + Soufriere Hills	15 Feb 1995 10 Aug 1995	-15, -1, -15 16	-78, 30, 168 -98, -62	17, 16, 16 16	7, 43, 25 81	S S
Peru + Colombia, Rabaul Soufriere Hills Soufriere Hills + Mexico, Rabaul Nyamuragira, Manam	10 Feb 1996 26 May 1996 18 Sep 1996 3 Dec 1996	-15, 5, -4 16 16, -4 -1, -5	-80, -80, 150 -62 -62, -98, 150 30, 145	17, 16, 16 16 16, 16 17, 17	65, 96 53 59, 28 45, 90	S S S S
Manam + Langila Popocatepetl Soufriere Hills, Philippines Soufriere Hills, Papua	11 Feb 1997 1 Jul 1997 20 Oct 1997 26 Dec 1997	-5 19 16, 16 16, -8	145 -98 -62, 121 -62, 150	17 16 15, 16 16, 16	107 32 36, 20 37, 22	S S S S
Tungurahua (?), Vanuatu Soufriere Hills Manam, Cerro Azul, Nyamuragira	2 Feb 1998 4 Jul 1998 7 Oct 1998	-1, -16 16 -5, 0, -1	-78, 168 -62 144, -90, 30	17, 16 16 17, 17, 16	98, 15 56 28, 39, 19	S S S
Guagua Pinch + Tungurahua, Vanuatu Cameroon Mayon, Colombia Soufriere Hills + Ulawun, Tungurahua + Guagua Pichincha	23 Jan 1999 31 Mar 1999 22 Jun 1999 24 Jul 1999 16 Nov 1999	-1, -16 4 13, 2 16 -5, -1	-78, 165 10 124, -80 -62 150, -78	17, 16 16 17, 16 17 17	75, 49 63 41, 46 42 31, 51	S S S S S
Vanuatu, Nyamuragira, Tungurahua Mayon + Vanuatu, Tungurahua	4 Feb 2000 29 Feb 2000	-16, -1, 0 13, -16, -1	165, 30, -78 124, 168, -78	17, 16, 16 16, 16, 16	33, 41, 12 25, 32	S S

Volcano or region	Time	Latitude (°)	Longitude (°)	Altitude (km)	SO ₂ (kt)	Instrument
Ulawun (+ Miyakejima)	26 Sep 2000	-5	150	17	42	S
Nyamuragira, Mayon(?)	13 Feb 2001	-1, 13	30, 124	16, 18	47, 88	S
Ulawun	29 Apr 2001	-5	150	16	41	S
Mayon, Lopevi	23 Jun 2001	13, -16	124, 168	16, 16	49, 22	S
Tungurahua, Soufriere Hills	7 Aug 2001	0, 16	-78, -62	16, 16	29, 46	S
Africa, Tungurahua +	25 Sep 2001	-1, 0	30, -78	16, 16	31, 47	S
Tungurahua (+ Manam), Nyiragongo	14 Jan 2002	-1(-4), -1	-78(144), 30	17, 15	83, 19	S
Tungurahua (+ Africa)	20 Mar 2002	-1	-78 (30)	17	77	S
<i>Nyamuragira</i>	23 Jul 2002	-1	30	15	23	M
<i>Witori</i>	2 Aug 2002	-6	150	14	18	M
<i>Ruang</i>	26 Sep 2002	2	125	18	71	M, G
<i>El Reventador</i>	5 Nov 2002	0	-78	17	77	M, G
<i>Nyiragongo, Lokon</i>	9 Jan 2003	-1, 1	30, 125	15, 16	12, 10	M, G
<i>Nyiragongo, Lokon (Rabaul?)</i>	5 Mar 2003	-5, 1	30, 125	17, 15	12, 13	M, G
<i>Anatahan, Nyiragongo, Ulawun</i>	14 May 2003	16, -1, -5	143, 30, 150	16, 16, 17	9, 15, 6	M
<i>Lewotobi, Kanlaon</i>	13 Jun 2003	-8, 10	123, 123	15, 15	9, 15	M, G
<i>Soufriere Hills</i>	13 Jul 2003	16	-62	17	41	M, G
<i>Gamalama, Japan</i>	17 Aug 2003	1, 33	128, 131	16, 16	8, 7	M, G
<i>Bezmyanny or Klyuchevskoy</i>	6 Sep 2003	56	160	14	8	G
<i>Lokon, Soufriere Hills + Masaya</i>	26 Sep 2003	2, 15	125, -62	16, 16	7, 5	M, G
<i>Rabaul</i>	10 Nov 2003	-5	150	16	17	M, G
<i>Rabaul</i>	5 Dec 2003	-5	150	16	13	M, G
<i>Rabaul, Nyiragongo?</i>	9 Jan 2004	-5, -1	150, 30	17, 15	11, 9	M, G
<i>Langila, Nyiragongo?</i>	3 Feb 2004	-5, -1	150, 30	17, 17	11, 3	M, G
<i>Soufriere Hills</i>	4 Mar 2004	10	-62	17	22	M, G
<i>Nyamuragira, Awu + Tengger</i>	12 Jun 2004	-1, 4, -8	30, 125, 112	17, 15	20, 18	G
<i>Pacaya, Galeras</i>	17 Jul 2004	15, 1	-91, -77	17, 17	11, 11	G
<i>Galeras</i>	11 Aug 2004	1	-77	16	15	G
<i>Vanuatu, Rinjani + Kerinci</i>	30 Sep 2004	-16, -8, -2	168, 116, 101	15, 15, 17	7, 15	G
<i>Manam, Soputan</i>	30 Oct 2004	-4, 1	144, 125	16, 16	8, 11	G
<i>Manam, Nyiragongo</i>	24 Nov 2004	-4, -1	144, 30	17, 15	18, 11	G
<i>Nyiragongo, Reventador</i>	4 Dec 2004	0, 0	30, -77	16, 16	19, 5	G
<i>Vanuatu, Soputan</i>	24 Dec 2004	-16, 1	168, 125	17, 15	15, 16	G
<i>Manam</i>	28 Jan 2005	-4	144	18	130	M, G
<i>Anatahan, (+)</i>	3 Apr 2005	16	143	15	15	M
<i>Anatahan, Soufriere Hills</i>	23 Apr 2005	16, 16	143, -62	16, 16	21, 21	M

Volcano or region	Time	Latitude (°)	Longitude (°)	Altitude (km)	SO ₂ (kt)	Instrument
<i>Anatahan, Fernadina, Vanuatu</i>	18 May 2005	16, 0, -16	143, -91, 168	15, 15, 15	8, 11, 6	M
<i>Anatahan, Santa Ana</i>	12 Jun 2005	16, 14	143, -90	15, 15	12, 9	M
<i>Anatahan, Soufriere Hills</i>	12 Jul 2005	16, 16	143, -62	15, 15	14, 10	M
<i>Anatahan, Raung</i>	6 Aug 2005	16, -8	143, 113	15, 15	13, 20	M
<i>Anatahan, Raung</i>	16 Aug 2005	16, -8	143, 113	15, 15	14, 17	M, G
<i>Santa Ana</i>	5 Oct 2005	14	-90	17	32	M
<i>Sierra Negra, Dabbahu</i>	25 Oct 2005	-1, -13	-91, 40	15, 15	16, 22	G
<i>Karthala, Galeras</i>	24 Nov 2005	-10, -2	43, -80	16, 16	13, 11	M, G
<i>Soputan, Lopevi</i>	24 Dec 2005	1, -16	125, 168	16, 16	23, 13	M, G
<i>Rabaul +</i>	23 Jan 2006	-5	152	16	25	G
<i>Manam, Chile</i>	4 Mar 2006	-5, -40	144, -70	17, 16	58, 6	G, T
<i>Cleveland</i>	14 Mar 2006	53	-170	13	8	G
<i>Ecuador, Tinakula, Lascar</i>	18 Apr 2006	-5, -10, -23	-78, 166, -68	17, 17, 17	13, 17, 3	M
<i>Soufriere Hills</i>	23 May 2006	16	-62	19	125	M, G, T
<i>Kanlaon</i>	2 Jul 2006	10	123	20	42	M
<i>Tungurahua, Rabaul</i>	16 Aug 2006	-2, -4	-78, 150	19, 17	40, 20	M, G, T
<i>Rabaul</i>	10 Oct 2006	-4	150	17	131	M, T
<i>Ubinas, Vanuatu</i>	25 Oct 2006	-20, -20	-70, 168	17, 15	8, 25	M
<i>Ambrym</i>	9 Nov 2006	-10	160	17	27	M, T
<i>Nyamuragira, Mexico</i>	29 Nov 2006	5, 5	30, -90	17, 15	28, 21	M, G, T
<i>Bulusan, Soputan, Vanuatu</i>	24 Dec 2006	13, 1, -16	125, 125, 168	18, 16, 15	8, 8, 14	M, G
<i>Karthala, Bulusan, Lascar,</i>	23 Jan 2007	-10, 13, -23,	43, 125, -68,	17, 17, 15,	5, 5, 6,	M, G, T
<i>Shiveluch, Vanuatu</i>		57, -16	160, 168	15, 15	7, 5	
<i>Nevado del Huila, Karthala, Vanuatu</i>	22 Feb 2007	0, -10, -16	-70, 43, 168	16, 15, 16	8, 10, 8	M, G, T
<i>Etna, Reventador, Ambrym</i>	24 Mar 2007	38, 0, -16	15, -78, 160	15, 16, 17	8, 17, 14	M, G, T
<i>Piton de la Fournaise, Reventador +</i>	8 Apr 2007	-20, 0	57, -80	16, 16	22, 11	M, G, T
<i>Ulawun, Vanuatu, Nevado del Huila</i>	3 May 2007	-5, -25, 3	150, 160, -70	15, 15, 15	11, 5, 6	M, G, T
<i>Papua, Kamchatka, Nyamuragira,</i>	13 May 2007	-10, 50, 0,	150, 150, 30,	16, 16, 16,	6, 1, 10,	M, G
<i>Ubinas + Lascar</i>		-20	-75	16	6	
<i>Llaima, Vanuatu, Bulusan</i>	23 May 2007	-30, -15, 13	-70, 160, 125	18, 15, 17	10, 6, 7	M, G
<i>Soputan, Bezymianny, Telica</i>	12 Jun 2007	1, 56, 13	125, 160, -87	16, 14, 15	13, 7, 9	M, G
<i>Lengai, Mexico</i>	2 Jul 2007	2, 20	29, -90	16, 15	14, 9	M
<i>Raung, Japan (+)</i>	27 Jul 2007	-5, 35	110, 130	15, 15	10, 10	M
<i>Manda Hararo, Java</i>	11 Aug 2007	12, -5	40, 115	17, 15	13, 14	M, T
<i>Vanuatu, Mexico</i>	20 Sep 2007	-5, 20	180, -90	16, 16	8, 13	M
<i>Jebel al Tair, Galeras</i>	5 Oct 2007	16, 1	42, -80	16, 16	41, 8	M, T

Volcano or region	Time	Latitude (°)	Longitude (°)	Altitude (km)	SO ₂ (kt)	Instrument
<i>Galeras, Jebel al Tair, Sopotan</i>	4 Nov 2007	-2, 15, -5	-80, 42, 110	16, 16, 16	7, 5, 8	M, G
<i>Sopotan or Krakatau, Galerias, Chikurachki</i>	14 Nov 2007	-5, -1, 50	110, -75, 155	16, 16, 15	9, 8, 10	M
<i>Talang, Galerias</i>	9 Dec 2007	0, 0	100, -75	16, 16	10, 12	M
<i>Ulawun?</i>	19 Dec 2007	1	150	17	17	M, G
<i>Nevado del Huila, Llaima</i>	3 Jan 2008	1, -35	-75, -71	17, 15	26, 4	M
<i>Galerias, Anatahan</i>	23 Jan 2008	-3, 15	-80, 145	16, 16	14, 7	M
<i>Tungurahua, Papua</i>	12 Feb 2008	-5, -5	-80, 155	16, 17	13, 10	M
<i>Batu Tara (+)</i>	13 Mar 2008	-5	125	16	26	M, G
<i>Lengai, Andes, Kerinic</i>	28 Mar 2008	-5, 5, -2	36, -80, 101	16, 16, 16	6, 4, 7	M
<i>Egon, Nevado del Huila</i>	12 Apr 2008	-5, 5	122, -76	15, 17	14, 9	M
<i>Mexico, Ibu, Chaiten</i>	27 Apr 2008	15, 1, -35	-90, 125, -70	16, 16, 16	9, 11, 3	M
<i>Mexico, Barren Island, Chaiten</i>	12 May 2008	10, 10, -35	-90, 90, -70	14, 16, 14	10, 14, 5	M
<i>Sopotan, Nicaragua/Costa Rica</i>	16 Jun 2008	1, 1	125, -85	16, 16	26, 8	M
<i>Okmok, Sopotan</i>	21 Jul 2008	53, 1	-168, 125	16, 16	51, 27	M
<i>Kasatochi</i>	15 Aug 2008	52	-175	17	273	M, G
<i>Dallafilla, Nevado del Huila, Reventador</i>	13 Nov 2008	14, 3	40, -78	17, 17	39, 28	M
<i>Karangetang, Galerias, Japan</i>	18 Dec 2008	3, 0, 30	125, -80, 130	17, 17, 15	15, 10, 9	M, G
<i>Barren Island, Galerias</i>	2 Jan 2009	10, 3	90, -80	17, 15	10, 10	M
<i>Indonesia?, Galerias</i>	27 Jan 2009	-5, 0	100, -80	16, 16	12, 10	M
<i>Galerias, Villarrica, Karangetang, Vanuatu</i>	16 Feb 2009	-2, -35, 3, -16	-78, -75, 100, 168	16, 15, 16, 17	11, 6, 6, 7	M
<i>Redoubt, Galerias</i>	28 Mar 2009	60, 0	-155, -75	13, 15	61, 43	M
<i>Fernandina, Nyamuragira</i>	12 Apr 2009	0, 0	-90, 30	16, 16	12, 16	M
<i>Galerias + Reventador</i>	7 May 2009	0	-75	15	25	M
<i>Rinjani, Vanuatu, Reventador</i>	22 May 2009	-5, -15, 3	116, 165, -80	16, 16, 16	4, 4, 13	M
<i>Sarychev, Manda Hararo</i>	21 Jun 2009	48, 12	153, 40	16, 16	446, 82	M, G
<i>Vanuatu, Mayon, Galerias</i>	4 Oct 2009	-15, 13, 2	165, 120, -80	17, 17, 17	4, 6, 10	M
<i>Tungurahua, Hawaii, Vanuatu</i>	19 Oct 2009	5, 20, -16	-76, -155, 165	16, 16, 16	7, 5, 5	M, G
<i>Galerias, Karkar, Vanuatu</i>	3 Dec 2009	0, -5, -16	-78, 146, 165	17, 17, 17	12, 10, 4	M
<i>Mayon, Nyamuragira, Vanuatu</i>	2 Jan 2010	13, 0, -15	120, 30, 168	16, 16, 16	8, 8, 9	M
<i>Turrialba, Vanuatu</i>	17 Jan 2010	5, -15	-82, 168	16, 16	9, 9	M
<i>Soufriere Hills</i>	16 Feb 2010	16	-62	17	36	M
<i>Arenal, Indonesia, Vanuatu</i>	2 Apr 2010	9, 0, -16	-84, 120, 168	15, 15, 15	14, 12, 5	M
<i>Tungurahua, Dukono, Vanuatu</i>	2 May 2010	-5, 2, -16	-78, 128, 168	16, 16, 16	14, 10, 7	M
<i>Pacaya, Ulawun, Sarigan</i>	6 Jun 2010	15, -5, 16	-91, 150, 145	17, 16, 15	27, 6, 4	M
<i>Ulawun, Costa Rica, Miyakejima</i>	16 Jul 2010	-5, 15, 35	150, -87, 140	16, 16, 16	8, 13, 6	M, G
<i>Karangetang, Nicaragua, Vanuatu</i>	15 Aug 2010	3, 15, -16	125, -85, 168	16, 16, 16	12, 12, 6	M

Volcano or region	Time	Latitude (°)	Longitude (°)	Altitude (km)	SO ₂ (kt)	Instrument
<i>Galeras, Sinabung</i>	30 Aug 2010	5, 5	-77, 100	16, 16	10, 12	M
<i>Karagetang, Barren Island</i>	4 Oct 2010	3, 12	125, 94	16, 16	20, 13	M
<i>Merapi</i>	8 Nov 2010	-7	110	17	97	M
<i>Tengger, Tungurahua, Chile</i>	23 Dec 2010	-8, -3, -40	110, -78, -75	17, 17, 17	16, 13, 8	M
<i>Tengger</i>	7 Jan 2011	-8	110	16	24	M
<i>Lokon, Planchon, Bulusan</i>	26 Feb 2011	1, -35, 13	125, -75, 125	16, 15, 16	13, 4, 12	M
<i>Karangrtang, Sangay, Planchon</i>	23 Mar 2011	2, -2, -35	125, -78, -75	15, 15, 15	10, 10, 5	M
<i>Galeras?, Karangetang</i>	12 Apr 2011	5, 5	-77, 128	16, 16	10, 9	M
<i>Tungurahua, Dukono, Vanuatu</i>	2 May 2011	2, 2, -16	-78, 128, 160	16, 16, 15	13, 9, 5	M
<i>Grimsvötn, Lokon</i>	27 May 2011	65, 1	-20, 125	14, 16	18, 27	M
<i>Puyehue</i>	11 Jun 2011	-41	-71	13	23	G
<i>Nabro</i>	21 Jun 2011	13	41	18	406	M, G
<i>Soputan, Marapi</i>	20 Aug 2011	1, 0	125, 100	18, 16	9, 3	M, G
<i>Manam, Tungurahua</i>	19 Oct 2011	-4, -3	144, -78	16, 16	8, 8	M
<i>Nyamuragira</i>	18 Nov 2011	-2	29	16	31	M
<i>Gamalama, Nyamuragira</i>	18 Dec 2011	1, -1	128, 29	16, 15	19, 13	M
<i>Vanuatu, Nyamuragira</i>	12 Jan 2012	-16, -1	168, 29	16, 14	14, 12	M
<i>Vanuatu, Nyamuragira</i>	11 Feb 2012	-16, -1	168, 29	17, 17	16, 15	M
<i>Nevado del Ruiz, Marapi</i>	12 Mar 2012	-3, 0	-76, 100	16, 17	12, 15	M
<i>Nyamuragira, Mexico</i>	7 Jun 2012	-1, 20	29, -95	16, 15	30, 4	O
<i>Soputan, Nevado del Ruiz, Mexico</i>	27 Aug 2012	1, 5, 20	124,-76,-95	16, 16, 15	30, 15, 5	O
<i>Nyamuragira, Mexico, Peru</i>	14 Oct 2012	-1, 20, -20	29, -95, -70	16, 16, 15	40, 15, 10	O
<i>Nyamuragira, Paluweh, Nevado del Ruizz</i>	7 Nov 2012	-1, -8, 5	29, 122, -76	15, 16, 17	20, 30, 17	O
<i>Copahue, Lokon +</i>	22 Dec 2012	-38, 1	-71, 125	15, 17	10, 45	O
<i>Paluweh, Karkar</i>	3 Feb 2013	-8, -5	122, 145	16, 17	25, 22	O
<i>Karkar, Vanuatu (+?)</i>	10 Mar 2013	-5, -16	145, 168	17, 16	24, 20	O
<i>Rabaul, Nevado del Ruiz, Nyamuragira</i>	18 Apr 2013	-3, 5, -1	150,-76, 29	17, 17, 16	40, 9, 20	O
<i>Mayon, Turrialba, Pavlof</i>	8 May 2013	13, 10, 55	124, -84, -162	17, 16, 14	35, 24, 6	O
<i>Rabaul, Mexico</i>	10 Jul 2013	-3, 20	150, -95	16, 15	30, 15	O
<i>Pacaya</i>	15 Aug 2013	15	-91	16	43	O
<i>Sinabung, Ubinas</i>	15 Sep 2013	3, -16	98, -71	17, 15	35, 8	O
<i>Merapi, Nyamuragira, Pacaya</i>	18 Nov 2013	-7, -1, 15	110, 29, -91	17, 17, 15	30, 13, 8	O
<i>Sinabung, Nyamuragira</i>	9 Dec 2013	3, -1	98, 29	17, 16	26, 15	O
<i>Sinabung +</i>	11 Jan 2014	3	98	16	29	O
<i>Kelut</i>	15 Feb 2014	-8	112	20	170	O
<i>Merapi, Tungurahua</i>	27 Mar 2014	-7, -1	110, -78	16, 16	31, 33	O

Volcano or region	Time	Latitude (°)	Longitude (°)	Altitude (km)	SO ₂ (kt)	Instrument
Santa Maria, Semeru	9 May 2014	15, -8	-91, 113	16, 16	25, 39	O
Sangeang-Api	31 May 2014	-8	119	17	60	O
Nyamuragira, Pavlof, Fuego, Dukono (Tungurahua)	9 Jul 2014	-1, 55, 14, 2	29, -162, -91, 128	16, 15, 15, 16	20, 10, 12, 20	O
Rabaul, Fuego	29 Aug 2014	-3, 14	150, -91	16, 16	36, 20	O
Nyamuragira	11 Sep 2014	-1	29	15	30	O
Ontakesan	27 Sep 2014	36	137	17	34	O
Sinabung, Turrialba	23 Oct 2014	3, 10	98, -84	17, 16	34, 17	O
Fogo, Semeru, Ubinas	24 Nov 2014	15, -8, -16	-24, 113, -71	17, 17, 16	11, 33, 11	O
Nevado del Ruiz, Nyamuragira, Vanuatu	16 Dec 2014	5, -1, -16	-76, 29, 168	15, 17, 16	8, 12, 21	O
Nyamuragira, Vanuatu, Honga Tonga	14 Jan 2015	-1, -16, -21	29, 168, -175	16, 16, 15	21, 17, 13	O
Vanuatu, Nyamuragira, Sopotan	16 Feb 2015	-16, -1, 1	168, 29, 124	17, 16, 16	13, 13, 13	O
Sopotan, Nevado del Ruiz, Santa Maria, Villarrica	8 Mar 2015	1, 5, 15, -39	125,-76,-91,-72	17, 16, 15, 15	14, 14, 8, 5	O
Tungurahua?, Batu Tara?	5 Apr 2015	-1, -8	-78, 124	17, 17	17, 22	O
Calbuco	25 Apr 2015	-41	-73	18	292	O
Manam, Tungurahua?	8 May 2015	-4, -1	144, -78	17, 17	24, 25	O
Wolf, Aira + Kuchinoerabujima	26 May 2015	0, 32, 30	-91, 131, 130	16, 15	63, 20	O
Raung	4 Jul 2015	-5	110	17	27	O
Cotopaxi, Raung, Suwanosjima, Manam	14 Aug 2015	0, -5, 30, -4	-80,110,130,144	16, 16, 16, 20	24,18,10,16	O
Nev. Ruiz + Reventador, Fuego, Sumatra	21 Sep 2015	5, 14, 3	-76, -91, 98	16, 17, 16	13, 8, 19	O
Sinabung, Fuego, Cotopaxi, Copahue	15 Oct 2015	3, 14, 0, -38	98, -91, -80, -71	16, 17, 15, 15	30, 15, 6, 13	O
Lascar, Sinabung, Nyamuragira, Fuego	30 Oct 2015	-23, 3, -1, 14	-70, 98, 29, -91	17, 17, 16, 16	13,17,12,17	O
Vanuatu, Tungurahua, Telica, Rinjani	17 Nov 2015	-16, -1,13, -5	168,-78,-87,116	18, 17, 17, 16	18,20,10,18	O
Vanuatu, Reventador, Tengger	5 Dec 2015	-16, 0, 2	168, -78, 120	17, 16, 16	16, 15, 12	O
Reventador, Sinabung	18 Dec 2015	0, 3	-78, 100	17, 16	16, 16	O
Sopotan +, Reventador, Fuego	8 Jan 2016	1, 0, 14	125, -78, -91	16, 17, 14	25, 19, 5	O
Semeru, Fuego	10 Feb 2016	-8, 14	113, -91	17, 16	34, 25	O
Vanuatu +, Tungurahua	27 Feb 2016	-16, -1	168, -78	16, 16	24, 16	O
Tungurahua, Sinabung +, Pavlof	15 Mar 2016	-1, 3, 55	-78, 98, -162	16, 17, 15	23, 26, 7	O
Reventador, Sinabung +, Fuego, Aira	13 Apr 2016	0, 3, 14, 32	-78, 98, -91, 131	17, 16, 15, 15	18, 30, 17, 6	O
Fuego, Nyamuragira + Ecuador, Langila, Sinabung	7 May 2016	14, -1, -5, 3	-91, 29, 150, 98	16, 17, 16, 17	16, 18, 16, 26	O
Bulusan, Sinabung, Semeru, Mexico	10 Jun 2016	13, 3, 8, 15	125,98,113,-100	17, 16, 17, 16	16,14,16,10	O
Rinjani, Sinabung, Santa Maria	1 Aug 2016	-5, 3, 15	116, 98, -91	16, 16, 16	10, 30, 24	O
Sinabung + Vanuatu, Fuego	28 Aug 2016	-16, 14	168, -91	16, 16	42, 23	O

Volcano or region	Time	Latitude (°)	Longitude (°)	Altitude (km)	SO ₂ (kt)	Instrument
Ubinas, Sinabung	3 Oct 2016	-16, 3	-71, 98	15, 16	16, 26	O
Sabancaya, Sinabung + Bulusan	5 Nov 2016	-16, 3	-72, 98	16, 16	38, 46	O
Dukono, Vanuatu, Sabancaya	12 Dec 2016	2, -16, -16	128, 168, -72	17, 18, 15	30, 28, 28	O
Sabancaya, Reventador, Sinabung + Vanuatu	10 Jan 2017	-16, 0, 3	-72, -78, 98	16, 17, 17	20, 30, 23	O
Sabancaya, Colima, Sinabung	4 Feb 2017	-16, 19, 3	-72, -104, 98	15, 16, 16	17, 15, 25	O
Sabancaya, Dukono, Fuego, Manam + Vanuatu, Bogoslof, Nevados de Chillán	5 Mar 2017	-16, 2, 14, -16, 53, -37	-72, 128, -91, 168, -170, -71	16, 17, 17, 17, 15, 15	10, 18, 8, 28, 4, 5	O
Sabancaya, Nevado del Ruiz, Sinabung, Vanuatu, Klyuchevskoy	10 Apr 2017	-16, 5, 3, -16, 56	-72, -75, 98, 168, 160	16, 16, 16, 16, 15	8, 15, 19, 17, 2	O
Sinabung, Manam, Fuego	5 May 2017	3, -4, 14	98, 145, -91	16, 17, 17	26, 10, 19	O
Sheveluch + Bogoslof	19 May 2017	57	161	15	20	O
Santa Maria, Sheveluch +, Manam	16 Jun 2017	15, 57, -4	-91, 161, 145	16, 16, 15	11, 33, 6	O
Fuego, Sinabung +, Sheveluch +	5 Jul 2017	14, 3, 57	-91, 98, 161	15, 16, 15	22, 21, 4	O
Sinabung, Cristobal + Fuego, Sheveluch + Bogoslof	8 Aug 2017	3, 13, 54	98, -87, -168	16, 17, 16 (26?)	31, 27, 5	O
Tinakula, Ambae	21 Oct 2017	-10, -15	166, 168	15, 15	60	O
Agung, Ambae, Sabancaya	27 Nov 2017	-8, -15, -5	116, 168, -80	15, 16, 15	22, 7, 12	O
Mayon, Vanuatu, Sabancaya	22 Jan 2018	13, -15, -5	124, 168, -80	15, 17, 16	7, 20, 16	O
Fuego, Vanuatu	1 Feb 2018	14, -15	-91, 168	16, 16	20, 17	O
Sinabung, Vanuatu	19 Feb 2018	3, -15	98, 168	16, 16	14, 21	O
Ambae, Vanuatu	26 Mar 2018	-15	168	16	60	O
Ambae	6 Apr 2018	-15	168	17	91	O
Sabancaya	15 May 2018	-16	-72	16	16	O, T
Fuego	3 Jun 2018	14	-91	16	15	O, T
Fernandina	17 Jun 2018	0	-92	15	8	T
Agung, Sabancaya	28 Jun 2018	-8, -16	115, -72	17, 16	33, 23	O, T
Sierra Negra	8 Jul 2018	-1	-92	15	25	T
Ambae	20 Jul 2018	-15	168	17	228	O, T
Manam, Sabancaya	25 Aug 2018	-3, -16	144, -72	17, 16	25, 12	O, T
Krakatau, Sabancaya	23 Sep 2018	-6, -16	105, -72	16, 16	5, 11	O
Manam, Soputan, Reventador + Sangay	4 Oct 2018	-3, 1, 0	144, 125, -78	16, 16, 16	7, 4, 22	O
Nev.Ruiz, Sabancaya	24 Oct 2018	5, -16	-75, -72	16, 16	22, 11	O
Fuego, Sabancaya, Krakatau	6 Nov 2018	14, -16, -6	-91, -72, 105	16, 16, 15	10, 16, 19	O
Fuego, Sabancaya, Bagana	26 Nov 2018	14, -16, -6	-91, -72, 155	16, 16, 16	8, 9, 12	O
Sabancaya, Manam, Soputan, Vanuatu	8 Dec 2018	-16, -3, 1, -16	-72, 144, 125, 168	16, 17, 16, 15	24, 8, 4, 6	O

Volcano or region	Time	Latitude (°)	Longitude (°)	Altitude (km)	SO ₂ (kt)	Instrument
Krakatau, Vanuatu, Sabancaya	23 Dec 2018	-6, -16, -16	105, 168, -72	16, 15, 16	7, 6, 20	O
Krakatau, Sabancay, Manam	4 Jan 2019	-6, -16, -3	105, -72, 144	17, 17, 16	5, 20, 9	O
Manam, Sabancaya	24 Jan 2019	-3, -16	144, -72	17, 16	23, 14	O
Manam, Sabancaya	14 Feb 2019	-3, -16	144, -72	16, 16	12, 13	O
Manam, Sabancaya, Mexico, Chile	19 Mar 2019	-3,-16,18,-24	144,-72,-98,-68	17, 16, 18, 15	9, 12, 6, 7	O
Sabancaya, Manam, Nev.Ruiz, Gamalama	20 Apr 2019	-16, -3, 5, 1	-72, 144,-75,128	17, 16, 16, 16	31, 12, 15, 7	O, T
Sinabung, Manam, Sabancaya	25 May 2019	3, -3, -16	98, 144, -72	17, 16, 16	11, 20, 21	O, T
Raikoke	22 Jun 2019	48	153	17	196	O
Raikoke, Ulawun	29 Jun 2019	48, -5	153, 151	15, 19	221, 107	O, T
Ubinas, Raikoke, Manam	19 Jul 2019	-16, 48, -3	-71, 153, 144	15, 16, 17	72, 141, 15	O, T
Ulawun, Mexico	3 Aug 2019	-5, 20	151, -100	19, 17	111, 12	O
Ubinas	16 Aug 2019	-16	-71	16	27	O, T

Table 2: Inventory of volcanic SO₂ emissions into the stratosphere integrated above 14 km in low latitudes, 13 km in mid-latitudes and 12 km in high latitudes. Listed altitudes and latitudes represent the region of maximum injection (or perturbation). Derived from satellite data (2002–2012) by MIPAS (M) and GOMOS (G). Based on a previous study from Brühl et al. (2018) with scaling factors for T63 and already published in an earlier version in Bingen et al. (2017) (*in italics*). Extended with satellite data from SAGE II(V7.00) (S) back to 1990–2002, and from 2012–2019 by OSIRIS (O). Sometimes also TOMS/OMI/OMPS (T) are used for handling data gaps. For detailed description see the text. Data available online in Fortran formatted form and as netcdf (https://doi.org/10.26050/WDC/SSIRC_3).

5 Implementation of SO₂ emissions into the EMAC Model

The amount of SO₂ injected from each volcanic eruption is calculated by integrating the vertical SO₂ profiles, described in Table 2. Then, the SO₂ plumes are incorporated into the model simulations by adding the satellite-derived 3-dimensional perturbations of SO₂ mixing ratios to the simulated SO₂ at the time of the eruptions. In order to get the correct altitude distribution and to reduce additional errors caused by the low temporal resolution of the satellite data and possible numerical problems due to huge gradients or values out the range of used procedures in the model, we did not implement the volcanic SO₂ emissions as point sources.

Effusive eruptions and quiescent degassing volcanoes from the time-dependent monthly 3D climatology of Diehl et al. (2012) were added to the tropospheric SO₂ background emissions in the model simulations and truncated at an altitude of 200 hPa to avoid double counting in the stratosphere and uppermost troposphere since the original climatology also contains contributions of explosive volcanoes listed in Table 2 (only 1990 to 2009) in a crude way (Brühl et al., 2018). In some cases,

especially in the tropics, some SO₂ from degassing is transported by convection to the lowermost stratosphere (see e.g. 1998 in Figure 6).

295 The SO₂ emissions of the volcanic sulfur emission inventory are used in the EMAC model simulations, resulting in the time series shown in Figure 6, with mixing ratios between background conditions of a minimum of 0.001 ppbv (parts per billion by volume (10^{-9})) in volcanically quiescent periods, and highly active volcanic conditions with a maximum of 114 ppbv (as indicated at the top of the colour key, 5-day average) after the Pinatubo eruption. In the Junge-aerosol layer (i.e. around 25 to 29 km), typical mixing ratios of SO₂ are about 0.03 ppbv.

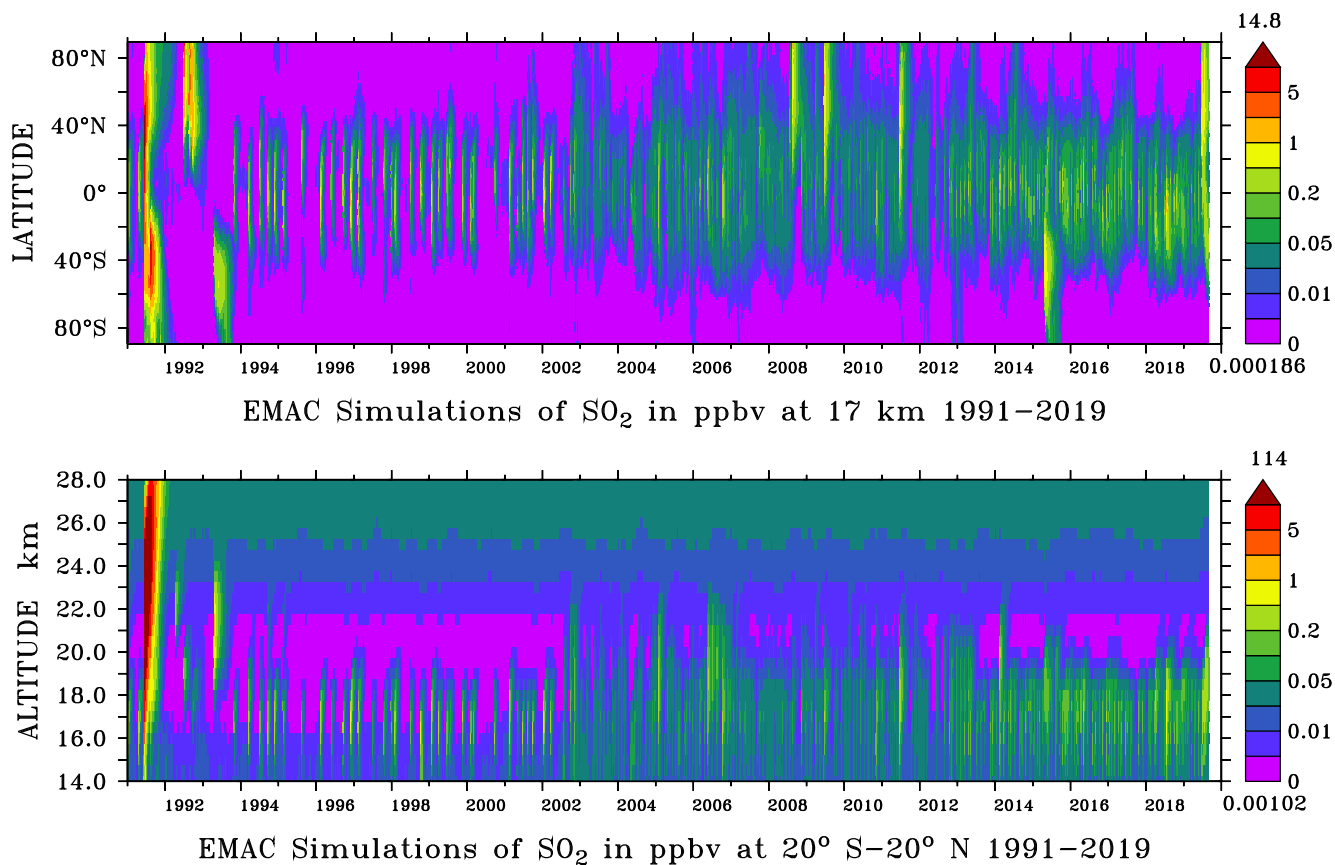


Figure 6. EMAC simulation of the stratospheric SO₂ mixing ratios (ppbv) (January 1991–August 2019) from the volcanic sulfur emission inventory (Table 2), in horizontal T63 resolution at 17 km altitude (top) and in vertical distribution for tropical regions 20° S–20° N (bottom). Maximum and minimum values are indicated above (dark red) and below (violet) the colour keys, respectively.

300 The volcanic eruptions in 1990 are included into the model during the spin-up phase of the model simulations (not shown), with the emissions of the first entry in Table 2 set to the upper limit consistent to the Smithsonian reports, SAGE and TOMS. The low number of volcanic eruptions in 1991 and the following years is due to the low coverage of satellite data and "saturation" effects of the satellite instrument (See subsection 2.4 about SAGE). The signatures of medium and small volcanic eruptions are

too weak to be seen during the high concentrations in the first years after the Pinatubo eruption. There are also less entries in the Smithsonian database. From 2002 onwards, a higher number of small volcanic eruptions is captured in the volcanic sulfur emission inventory. This is rather due to the improved data coverage enabled by a larger number of satellite instruments, than to higher volcanic activity.

In most cases, the stratospheric SO₂ mixing ratios are highest at tropical latitudes. For this reason, tropical regions (20° S–20° N) are chosen for the vertical distribution in the lower illustration of Figure 6 and subsequent figures. Exceptions to this typical SO₂ pattern are single medium strong volcanic eruptions at high latitudes like Kasatochi (2008), Sarychev (2009) and Raikoke (2019) in the northern hemisphere or Calbuco (2015) in the southern hemisphere. Another noteworthy case is the Nabro (2011) eruption, where the volcanic emissions were transported from the tropics to northern latitudes by the Asian monsoon circulation (Clarisse et al., 2014).

MIPAS typically captures background SO₂ mixing ratios in the lowermost tropical stratosphere at 16 km to 17 km of around 0.02 ppbv to 0.05 ppbv (Figure 1), which can be reproduced by the model only if many more volcanoes are considered than listed in the National Aeronautics and Space Administration (NASA) SO₂ database (Brühl et al., 2015). Some time periods with low volcanic activity resulting in stratospheric background conditions can be identified between 1996 and 2004. To reach realistic SO₂ mixing ratios in the lower tropical stratosphere during these years, the oxidation of DMS and other sulfur species is needed. The lower panel of Figure 6 shows increasing SO₂ with altitudes of above 23 km due to additional production from OCS photolysis.

The comparison of the simulated and observed SO₂ values shows that the volcanic SO₂ emissions from the volcanic sulfur emission inventory in Table 2 correlate well with the peaks of the mixing ratios in Figure 6, as they dominate the stratospheric sulfur burden. In the stratosphere, SO₂ is converted to sulfate aerosol, which explains most of the interannual variability of the stratospheric aerosol burden as well as its influence on the stratospheric radiation. Generally, the conversion of SO₂ to sulfate aerosol particles depends on several factors, such as the altitude, latitude, or season of the eruption and takes according to Höpfner et al. (2015) about 13, 23 and 32 days in 10–14, 14–18 and 18–22 km altitude, respectively, in midlatitudes. Carn et al. (2016) report an e-folding time varying between 2–40 days. The range agrees with our simulations (and assumptions in section 4). Enhanced SO₂ concentrations from Pinatubo via photolysis of gaseous H₂SO₄ remained in the mesosphere for several years (Brühl et al., 2015; Rinsland et al., 1995).

330 **6 Climate impact of stratospheric aerosol in EMAC simulations**

We compared the global influence of sulfur emissions on different atmospheric optical parameters. Based on Mie-theory-lookup tables, optical properties such as optical depths, single scattering albedos and asymmetry factors, which are used in radiative transfer simulations, were calculated online for different aerosol types: sulfate, dust, organic carbon and black carbon, sea salt, and aerosol water (Dietmüller et al., 2016). Via multiple calls of the radiation module RAD with and without aerosol the influence of stratospheric aerosol on instantaneous radiative forcing and heating is computed online (section 3). Also, the feedback to atmospheric dynamics is included.

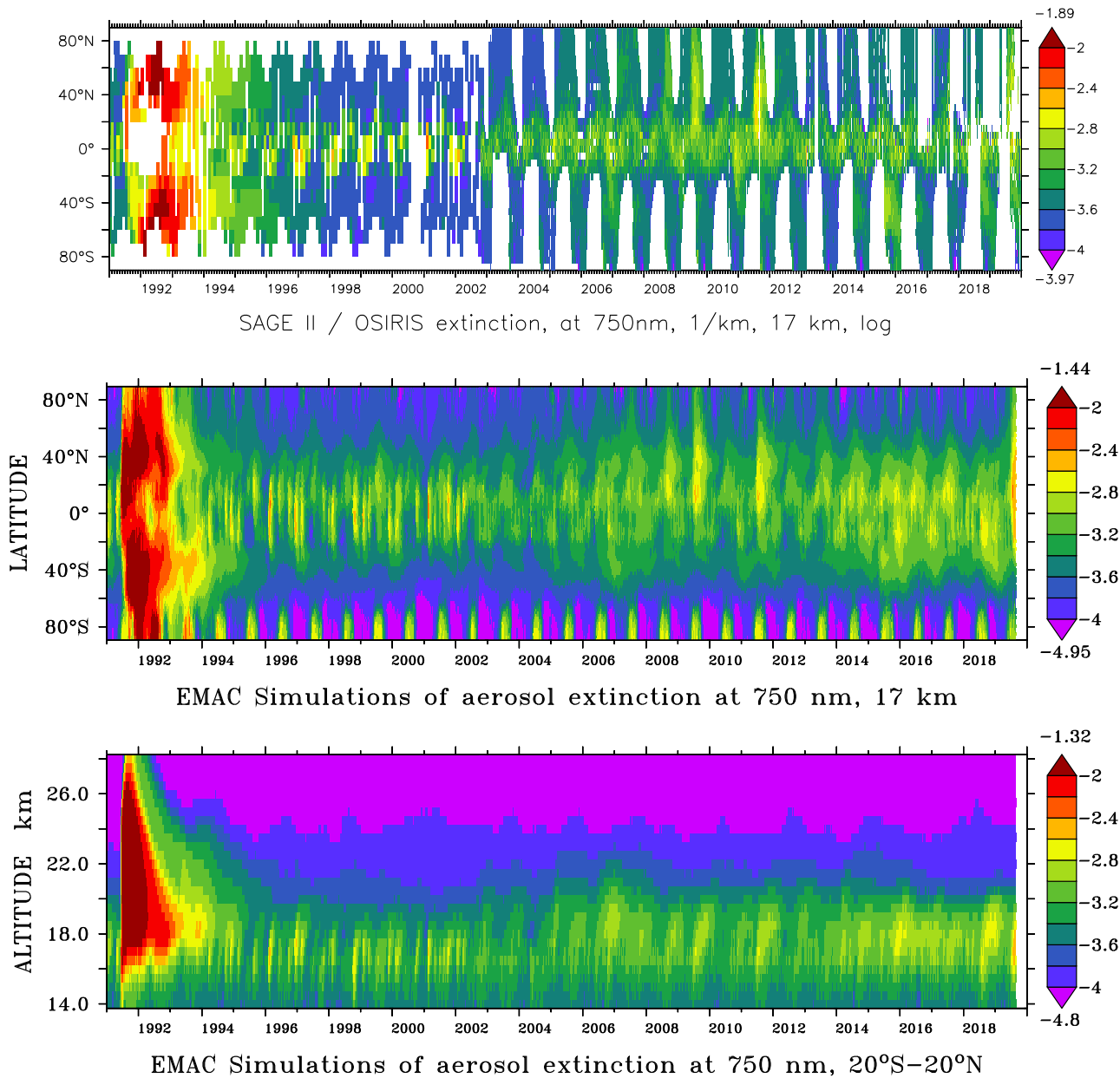


Figure 7. Comparison of aerosol extinction for 750 nm wavelength at 17 km altitude between the model simulations (lower panels) and SAGE II and OSIRIS satellite data (upper panel). EMAC simulation of the stratospheric aerosol extinction in logarithmic scale $\log(1/\text{km})$ for 750 nm wavelength from January 1991–August 2019 based on the volcanic sulfur emission inventory (Table 2), in horizontal T63 resolution of zonal mean at 17 km altitude (middle) and in vertical distribution for tropical regions 20° S–20° N (bottom). Maximum and minimum values appear above (dark red) and below (violet) the colour keys, respectively.

6.1 EMAC simulations of the stratospheric aerosol extinction

Figure 7 and Figure 8 show the global stratospheric aerosol extinction coefficients (in decadal logarithm) for the period 1991—2019 at 750 nm and 550 nm wavelengths of the EMAC model simulations at 17 km altitude and its vertical profile for tropical regions for 20° S–20° N. For medium eruptions, the maximum of the aerosol extinction lies at an altitude between 16 km and 18 km. For this reason, an altitude of 17 km is chosen in the following analyses.

Figure 7 contains also the extinctions observed by OSIRIS and SAGE (interpolated from the observations at 550 and 1025 nm). The strongest event in these model simulations is the Pinatubo (Table 2) eruption in 1991, which dominates the stratospheric aerosol extinction coefficient for more than three years after the eruption with a global distribution from the equator to the poles in both hemispheres and a maximum altitude of more than 26 km. All other eruptions are significantly smaller, and for this reason a logarithmic scale is chosen. For further comparisons at 750 nm with GOMOS and OSIRIS we refer to Figure 3, Figure 4 and Brühl et al. (2018).

The EMAC model simulations of the aerosol extinction coefficients at 550 nm (Figure 8) agree well with the satellite measurements of GOMOS (Figure 2) and SAGE II (Figure 5) for the aerosol layer at an altitude of 16–22 km where measured extinction values exceed $\approx 2 \times 10^{-4} \text{ km}^{-1}$. Above about 24 km EMAC is lower than the observations because in the model meteoric dust particles were not considered.

The two figures show a similar distribution of the aerosol extinction at wavelengths of 550 nm and 750 nm. Due to the typical size and composition of stratospheric aerosol particles, the aerosol extinction is higher at 550 nm than at 750 nm. The peaks caused by mineral dust particles during summer in the Northern subtropics are more pronounced at 750 nm than at 550 nm.

Despite the presence of volcanoes in the Antarctic (like Mount Erebus), the seasonal change of extinction coefficient is not due to volcanic eruptions, but to the presence of Polar Stratospheric Clouds (PSCs) as simulated by the model.

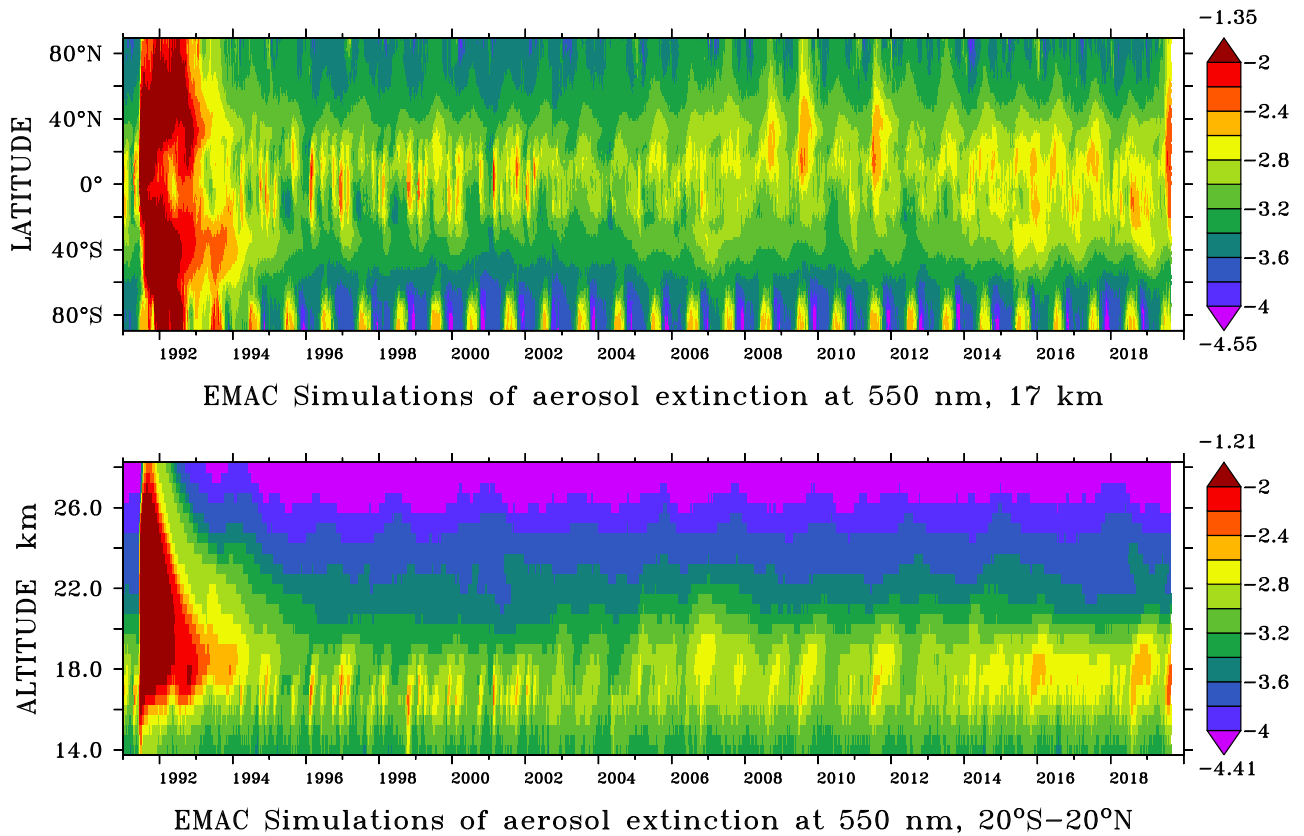


Figure 8. EMAC simulation of the stratospheric aerosol extinction in logarithmic scale $\log(1/\text{km})$ for 550 nm wavelength from January 1991–August 2019 based on the volcanic sulfur emission inventory (Table 2), in horizontal T63 resolution of zonal mean at 17 km altitude (top) and in vertical distribution for tropical regions 20° S–20° N (bottom). Maximum and minimum values appear above (dark red) and below (violet) the colour keys, respectively.

6.2 EMAC simulations of Aerosol Optical Depth (AOD)

The total stratospheric Aerosol Optical Depth (AOD) is obtained by the vertical integral of the aerosol extinction above an altitude of about 16 km (for mid-latitudes above about 14 km). The stratospheric AOD is shown on a logarithmic scale in Figure 9 and Figure 10 with the new model simulations (red line) compared to satellite observations (light blue, green, and blue lines). Using the wavelengths of the satellites in the calculations (Section 3) avoids introducing additional errors through the use of conversion factors to adjust the values between the different wavelengths.

From 1991 to 2012, SAGE II (light blue line), GOMOS (green line) and SAGE+CALIPSO and SAGE+OSIRIS (blue line) provide satellite data at a wavelength of 550 nm (Figure 9, OSIRIS data were converted from 750 nm by Glantz et al. (2014)). For convenience also GloSSAC (Kovilakam et al., 2020) is included as black line in the upper panel. Note the odd downward jump after 2012 which is not visible in OSIRIS data.

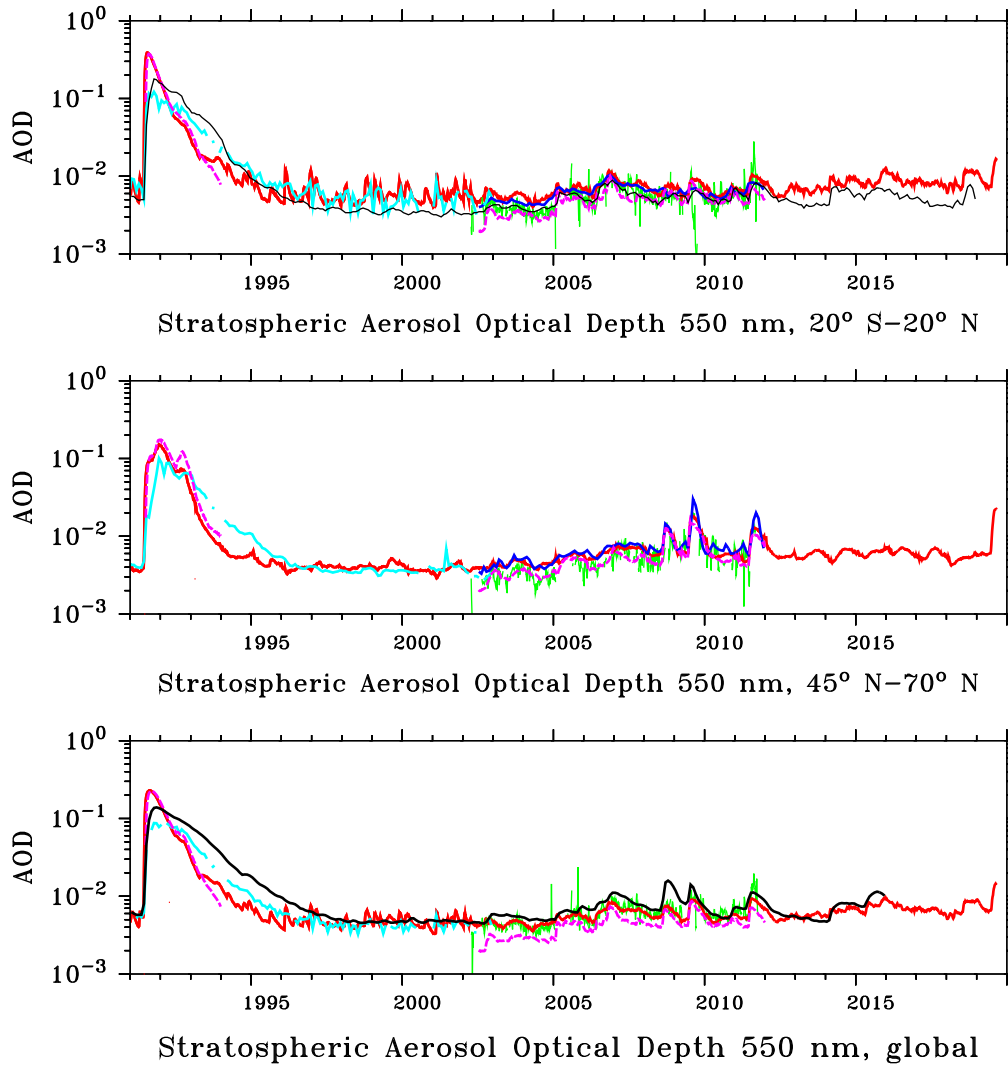


Figure 9. Stratospheric AOD at 550 nm wavelength: Tropical regions 20° S–20° N above 110 hPa are shown on the top, the northern hemisphere 45° N–70° N above 145 hPa is shown in the middle and global means at the bottom. Satellite observations from SAGE II (Thomason et al., 2008) are indicated by the light blue line, GOMOS (Bingen et al., 2017) by the green line and values derived from SAGE+CALIPSO (upper figure) (Santer et al., 2014) and SAGE+OSIRIS (middle figure) (Glantz et al., 2014) by the blue line. The red line shows the EMAC model simulations using the SO₂ injections of Table 2, compared to the simulations of Brühl et al. (2015) (pink dashed line) and the global stratospheric AOD from Schmidt et al. (2018) (black line in lower panel). The black line in the upper panel is from GloSSAC.

The maximum is reached after the Pinatubo eruption with a stratospheric AOD of 0.4 in the tropics (Figure 9 upper panel, EMAC), being an order of magnitude larger than the following medium eruptions with a stratospheric AOD of about 0.01 (e.g. Manam in early 1997, Rabaul in 2006 and Nabro in 2011). The differences after the large Pinatubo eruption in 1991 between

370 the model simulations and the SAGE II observations are related to the “saturation” effects of the satellite instrument (i.e. data
gaps due to an opaque path through the atmosphere at the tangent point) and can be observed for more than one year, (also
shown above in Figure 5). In this study about 17 Tg SO₂ are injected for the Pinatubo eruption (Guo et al., 2004). Model
comparisons by Timmreck et al. (2018) show that the span of used injections varies between 10 Tg SO₂ (e. g. Dhomse et al.
(2014); Mills et al. (2016); Schmidt et al. (2018)) and 20 Tg SO₂ (e.g. English et al. (2013)). Thus, this study is in the middle
375 range of the injected sulfur mass. On the other hand, filling the gaps in the SAGE data just by horizontal linear interpolation
increases the peak AOD by about a factor of 2, which is close to the GloSSAC compilation. In Figure 10 the AVHRR (Advanced
Very High Resolution Radiometer) by Long and Stowe (1994) at 630 nm are included, which are close to our simulations (if
converted to 750 nm their AOD would be slightly less or to 550 nm slightly larger). When comparing the EMAC simulations
(red line in Figure 9) with the simulation of Schmidt et al. (2018) (black line in Figure 9, lower panel) it can be recognized that
380 a smaller value for the peak of the Pinatubo eruption occurs, but here it needs to be considered that Schmidt et al. (2018) are
using monthly global-means. This has the consequence that the signal of single eruptions is blurred and smaller sized eruptions
cannot be easily identified.

Between 1993 and 1996 the reduction of the stratospheric AOD in the model simulations is faster than indicated by the
satellite observations and in Schmidt et al. (2018). This indicates that the removal of stratospheric aerosol is still too rapid
385 from applying the modal model. Schmidt et al. (2018) show a slower decrease in AOD after the Pinatubo eruption. This could
indicate that EMAC still needs better fine-tuning of the size distribution modes, or adding modes in the aerosol submodel to
improve the aerosol removal in the stratosphere. Here the sectional aerosol model used by Schmidt et al. (2018) might have
an advantage (Clyne et al., 2021). Additionally, smaller volcanic eruptions might be missing, in view of the low number of
identified events in the years after the Pinatubo eruption.

390 In Figure 10, the coverage of GOMOS (green line) is often too low at a wavelength of 750 nm for the years from 2002 to
2012, so the inclusion of OSIRIS data (blue line) is important (Brühl et al., 2018). For the years after 2012 the timeline only
contains data from OSIRIS at 750 nm wavelength.

Nevertheless, there still remain small differences between the model simulation and the observations, for instance in 2010,
which indicates missing volcanic eruptions (or an underestimation of the Merapi eruption by MIPAS compared to OSIRIS,
395 Appendix B).

The different distributions of the peaks in the upper and the lower panels is related to the latitude of the volcanic eruptions.
Emissions reaching the stratosphere from strong eruptions in the tropics are distributed by the Brewer-Dobson circulation over
the northern and southern hemisphere even to high latitudes, as in the cases of Soufriere Hills and Rabaul in 2006. However, if
an eruption takes place at high latitudes (such as for Redoubt 2009) or at mid-latitudes like Kasatochi (2008), Sarychev (2009)
400 or Raikoke (2019), most of the emissions stay in the northern hemisphere and the signal in the tropics is weaker. Our northern
hemisphere results for AOD of about 0.025 for Raikoke (550nm) agree within uncertainties with Kloss et al. (2021) who use
different satellites and different modelling approaches.

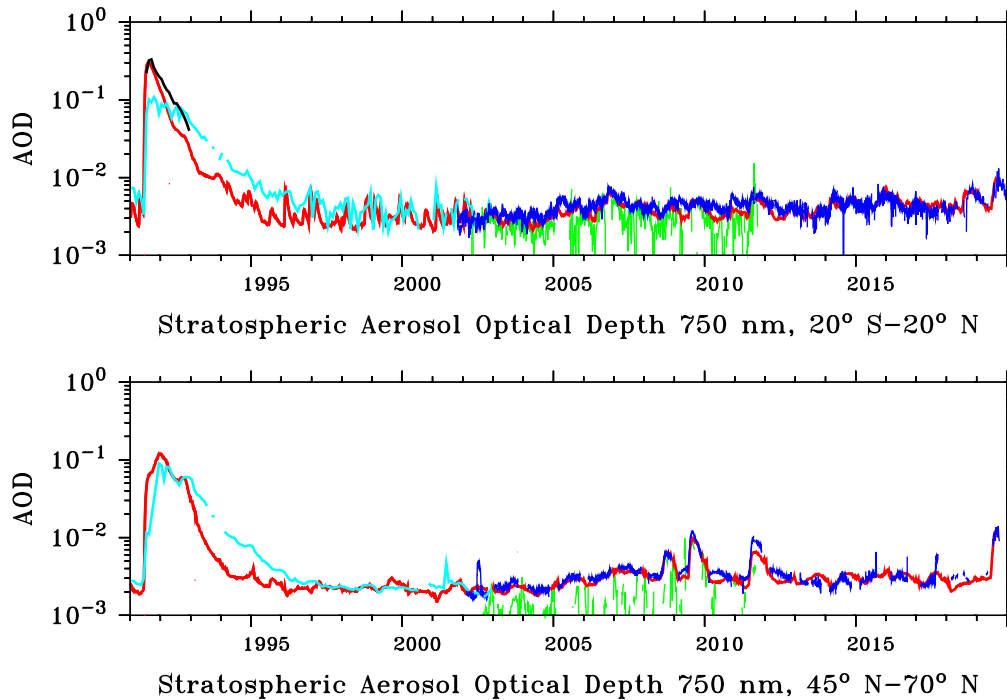


Figure 10. Stratospheric AOD at 750 nm wavelength: Tropical regions 20° S–20° N above 110 hPa are shown on the top and for the northern hemisphere 45° N–70° N above 145 hPa at the bottom. Satellite observations from OSIRIS (Rieger et al., 2019) are indicated by the blue line and GOMOS (Bingen et al., 2017) by the green line. For the Pinatubo period the black line shows the AVHRR observations by Long and Stowe (1994) at 630 nm (upper panel). The light blue line shows the interpolation of SAGE data at 550 nm and 1025 nm wavelengths. The EMAC model simulations, using the SO₂ injections of Table 2, are shown by the red line.

6.3 EMAC simulations comparing the radiative forcing at the tropopause

The instantaneous radiative forcing of the stratospheric aerosol is calculated by multiple calls of the RAD submodel (section 3).
 405 The simulated global negative radiative forcing in Wm^{-2} of stratospheric aerosol at the tropopause is illustrated in Figure 11.

As the Pinatubo eruption caused a negative radiative forcing of more than an order of magnitude greater than all other eruptions since then, the y-axis of the lower figure is plotted in inverted logarithmic scale; for instance, 10^0 corresponds to a global negative radiative forcing of 1.0 Wm^{-2} . The new model simulations with the additional volcanic eruptions (red line) are closer to the calculated estimates from satellite extinction measurements of SAGE, GOMOS and CALIOP by Solomon et al. (2011)
 410 (green bars) than in previous studies (e.g., Brühl et al. (2015) pink line). A comparison with data of total volcanic effective radiative forcing from (Schmidt et al., 2018) is shown by the black line. The large difference to our simulation in periods between medium sized eruptions shows that even medium- and small-sized volcanic eruptions can reach the stratosphere and have a significant influence on the global radiative forcing at the tropopause. In the period considered here, the volcanoes are the dominant factor in instantaneous global negative radiative forcing, with up to 0.2 Wm^{-2} for Rabaul and Nabro (2011)

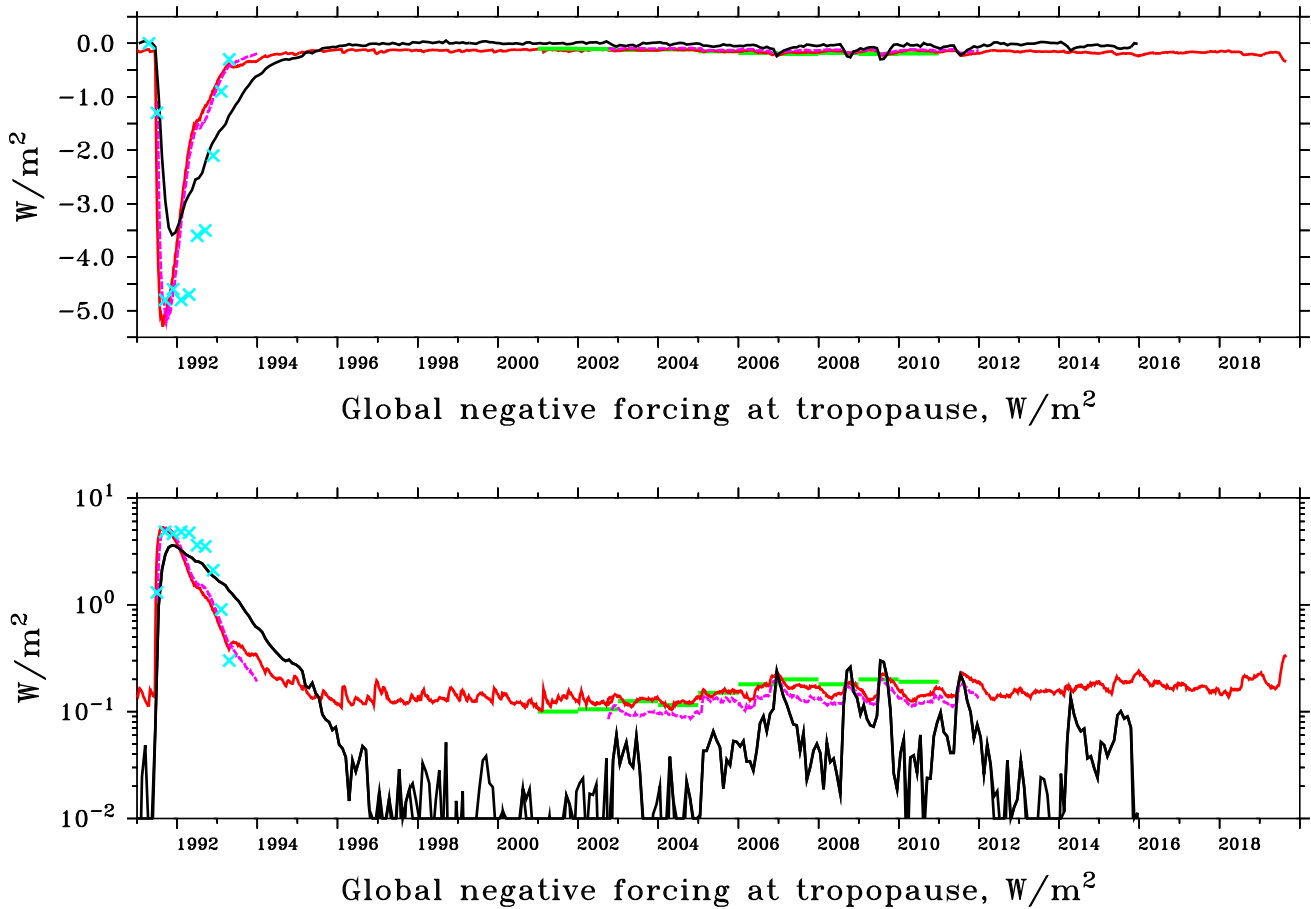


Figure 11. Global negative radiative forcing by stratospheric aerosol. Estimated averages for solar forcing at the top of the atmosphere from satellite observations of the Earth Radiation Budget Experiment (ERBE) (72-day means) (Wong et al., 2006; Tooney et al., 2011) are indicated by light blue crosses and annual averages derived from observations by Solomon et al. (2011) as green bars. The EMAC model simulations with instantaneous forcing at the tropopause (185 hPa, solar + IR) based on volcanic SO₂ emissions are represented by the red line, compared to the simulations of Brühl et al. (2015) (pink line) and data from Schmidt et al. (2018) with volcanic effective radiative forcing (black line).

415 and more than 0.3 Wm^{-2} for Raikoke/Ulawun (2019) compared to the volcanically quiescent period in 2002. The value for Raikoke/Ulawun is within the range discussed in Kloss et al. (2021). The strongest instantaneous global radiative forcing in the model simulations is caused by the Pinatubo eruption with a maximum of about -5 Wm^{-2} ; this is in good agreement with the results of Minnis et al. (1993) and the observations of the ERBE satellite (light blue crosses in Figure 11). A comparison between the ERBE observations (light blue crosses) and Schmidt et al. (2018) shows that they may underestimate the maxi-
 420 mum of the Pinatubo eruption 1991 but one has to keep in mind that ERBE sees only the solar forcing which is larger than total forcing. Schmidt et al. (2018) estimates the forcing from the difference of a simulation with and without Pinatubo, i.e.

including dynamical and chemical adjustments which leads to a smaller value than instantaneous forcing at the peak. A similar approach with EMAC leads to a peak forcing of about -4 Wm^{-2} (but with nudging of the troposphere in contrast to Schmidt et al. (2018) which leads to higher forcing here).

425 6.4 EMAC simulations of the stratospheric aerosol radiative heating

The simulated instantaneous aerosol radiative heating in the model is derived from multiple radiation calls with and without aerosol in the radiation submodel RAD. Aerosol formation is calculated by the GMXe submodel, while the aerosol optical properties are calculated by the AEROPT submodel.

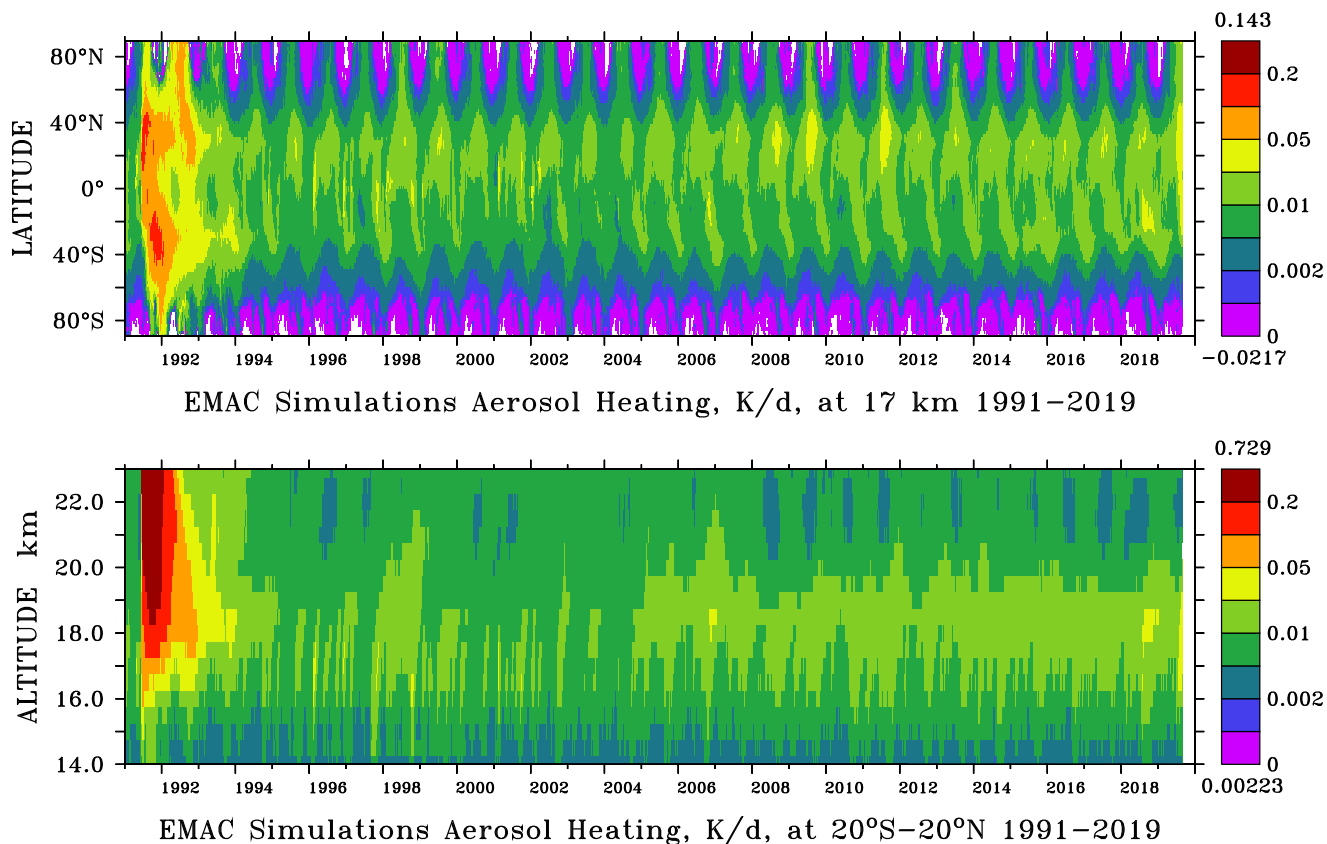


Figure 12. EMAC simulation of the aerosol radiative heating in K/day for solar and infrared radiation from January 1991–August 2019 based on the volcanic sulfur emission inventory (Table 2), in horizontal distribution at 17 km altitude (top) and in vertical distribution for tropical regions 20° S–20° N (bottom).

Figure 12 shows the calculated local heating effects in the stratospheric aerosol layer. Small and medium volcanic eruptions have the largest effects between altitudes of 17 km and 18 km and generate atmospheric heating of up to 0.03 K/day. The eruption of Pinatubo, on the other hand, had significantly stronger effects at altitudes of 20 km to 25 km and caused atmospheric

heating of more than 0.7 K/day, which corresponds quite well with the results of Rieger et al. (2020) showing a maximum of instantaneous solar heating rate of 0.5 K/day in the tropics near 24 km plus thermal heating rates of about 0.2–0.3 K/day. This is about 23 times greater than all other eruptions in the model simulation, including the Raikoke eruption in 2019.

435 Further, a seasonal signal contributes significantly to the radiative heating in the northern subtropics. This is caused by transport of desert dust to the UTLS mostly via the Asian summer monsoon convection, which generates additional heating during the time of the Asian summer monsoon (Brühl et al., 2018).

7 Discussion and conclusions

The objective of this study was to generate a detailed volcanic sulfur emission inventory and to improve the EMAC model simulations of the global stratospheric aerosol and sulfate burden, and compute the volcano-induced radiative forcing through validation with satellite data.

Updated OSIRIS data allowed us to extend the comparisons of Brühl et al. (2018) to 2019; a detailed analysis of L2 SAGE II data together with the Smithsonian volcano database was used to extend the comparison back to 1990. So the simulations in this paper encompass a total of 29 years and now covers the years 1991 to 2019, instead of 2002 to 2012 as in our previous work. Additional updated three-dimensional data sets are now available, which provide better temporal resolution than the commonly used monthly means of the MIPAS, GOMOS and OSIRIS instruments. The temporal resolution is now five days for the three instruments and it is possible to identify multiple volcanic eruptions within a short period of time. With the three-dimensional data sets, the vertical distribution of SO₂ can be distinguished and the amount of sulfur reaching the stratosphere can be calculated much more accurately than by estimation of a total column. To exclude tropospheric emissions and signals from high-altitude clouds, the integration of the sulfur emissions is set above an altitude of 12 km at high latitudes, 13 km at mid-latitudes and 14 km at low latitudes. To avoid double counting, tropospheric sulfur emissions are treated separately.

Our volcanic sulfur emission inventory is an improvement on the version published by Bingen et al. (2017) and Brühl et al. (2018). While the previous version included 230 explosive volcanic eruptions, the new version now lists more than 500 eruptions. An overview of these eruptions is given in the improved volcanic sulfur emission inventory in Table 2, which also includes the estimated stratospheric SO₂ emissions as well as the plume altitudes. These consist of about 80 eruptions in the first time period between 1990–2002 measured by the SAGE II instrument, 240 eruptions in 2002–2012 measured with multiple instruments and 230 eruptions in the last time period 2012–2019 measured by OSIRIS. The inclusion of many more small size eruptions reaching the UTLS has the consequence that stratospheric aerosol optical depth and radiative forcing does not decrease to almost zero between medium size eruptions, in agreement with observations, and in contrast to a previous work.

460 Strong volcanic eruptions can inject several teragrams of SO₂ directly into the stratosphere. For this reason, the maxima of the global stratospheric SO₂ concentrations correlate well with the eruption events of the volcanic sulfur emission inventory in Table 2. The SO₂ emissions of smaller volcanic eruptions can reach the lower stratosphere by convective transport through the tropical tropopause, which results in accumulation of sulfate aerosol in the lower stratosphere. This was demonstrated to be important for correctly modelling the AOD in volcanically quiescent periods.

465 Our analysis shows the importance of using multi-instrument satellite data sets to fill data gaps and to detect as many volcanic eruptions as possible. The optimal data coverage was in the time period from 2002 to 2012, for which simultaneous measurements from the MIPAS, GOMOS and OSIRIS instruments are available. For 2002 to 2005 this includes also SAGE II. The periods with simultaneous observations by MIPAS and the other instruments were used to develop and validate a method for estimating injected SO₂ and its distribution from extinction observations. The evaluation by the satellite data sets shows that
470 GOMOS is important for detecting volcanic eruptions in MIPAS data gaps and for a better attribution of individual eruptions. Consequently, the combination of MIPAS, GOMOS and OSIRIS data leads to better SO₂ input for calculating the radiative forcing in the chemistry climate model EMAC.

Large volcanic ash plumes can interfere with the SO₂ signal in satellite measurements, and satellites could be “blind” during the first few days or months after an eruption (Höpfner et al., 2015). However, most volcanic ash particles are relatively large
475 and sediment after some hours or days, so they have only minor climatic significance (Boucher, 2015) and are not discussed in detail here. There are, however, volcanoes (e.g. eruption of Kelut in 2014 (Zhu et al., 2020)) which emit small ash particles which can stay in the lower stratosphere for several months (Vernier et al., 2016). Moreover, it has been found that the model setup might have to be improved by including an additional aerosol mode to slow down the removal by sedimentation of stratospheric aerosol after big volcanic eruptions.

480 Some satellite data sets still contain data gaps and noise. Comparing the model results with OSIRIS data in the northern tropics (Figure 10) indicates that some volcanic events are still underestimated or missing in the volcanic sulfur emission inventory in the year 2010. This could also explain the differences between the model simulations and satellite observations from Solomon et al. (2011), indicated by green bars in Figure 11 of the radiative forcing in this year.

The model also includes mineral dust and organics from the troposphere transported up to the UTLS. The EMAC simulations
485 show a seasonal signal in the stratospheric AOD and an enhanced radiative heating in the northern hemisphere, induced by the convective transport of mineral dust to the UTLS in the Asian monsoon region. This is confirmed by satellite observations and studies by Klingmüller et al. (2018). The influence of wildfires and other biomass burning plumes on stratospheric AOD has increased in recent years (Fromm et al., 2019), and this effect should be included in the model to account for perturbations in organic and black carbon.

490 Frequent volcanic eruptions of moderate and small intensities, injecting sulfur gases to the upper troposphere and lower stratosphere, contribute significantly to the stratospheric aerosol layer through accumulation. These cause a global negative radiative forcing of 0.12 (0.22 to 0.08) Wm⁻² at the tropopause, for example in the case of the eruptions of Soufriere Hills/Rabaul (2006), Nabro (2011) and the combination of the Sinabung, Wolf and Calbuco eruptions (2015) with a radiative forcing of up to 0.13 Wm⁻², and 0.2 Wm⁻² for Raikoke/Ulawun (2019) compared to volcanically quiescent periods (e.g. in 2000 to 2002).

495 *Code and data availability.* The Modular Earth Submodel System (MESSy) is continuously developed and used by a consortium of institutions. The use of MESSy and access to the source code is licensed to all affiliates of institutions which are members of the MESSy Consortium. Institutions can become a member of the MESSy Consortium by signing the MESSy Memorandum of Understanding. More

information can be found on the MESSy Consortium website (<http://www.messy-interface.org>, MessyConsortium, 2017). The input data files and model output of EMAC used here are stored at DKRZ, Hamburg, the volcanic inventory and the output for radiative forcing also at
500 WDCC (https://doi.org/10.26050/WDCC/SSIRC_3).

For the MIPAS data we refer to <http://www.imk-asf.kit.edu/english/308.php>. The sulfur injections from the volcanoes were estimated utilizing the NASA SO₂ database at GSFC (<http://so2.gsfc.nasa.gov>) and the Smithsonian volcano database (<http://www.volcano.si.edu>).

Author contributions. JS, CBr and JL defined the scientific questions and scope of this work. JS and CBr conceived the idea and methodology used in this paper and carried out the model simulations and the analysis. MH provided the MIPAS data, CBi provided the GOMOS data
505 and LR provided the OSIRIS data. All authors participated in the scientific discussion in regard to satellite data in particular. JS wrote the manuscript, and all authors reviewed the manuscript and provided advice on the manuscript and figures.

Competing interests. The authors declare that they have no conflicts of interest.

Acknowledgements. The research leading to these results has received funding from the European Research Council under the European Union's Seventh Framework Programme (FP7/2007–2013)/ERC grant agreement 226144 as part of the StratoClim project and funding
510 from ESA Aerosol CCI (European Space Agency). There is a close collaboration within the SPARC/SSIRC (Stratosphere-troposphere Processes And their Role in Climate / Stratospheric Sulfur and its Role in Climate) stratospheric aerosol model intercomparison project (<http://www.sparc-ssirc.org>) concerning SO₂ injections derived from satellite data and model intercomparisons. The computations have been performed at the Mistral supercomputer at DKRZ, Hamburg, Germany. We thank Adam Bourassa, Larry Thomason and the GOMOS, MIPAS, OSIRIS, SAGE, the Copernicus Climate Change Service (projects C3S_312a_Lot5 and C3S_312b_Lot2), and EOSDIS (NASA)
515 teams for their productive cooperation and providing their satellite data sets. GloSSAC (V2) data were obtained from the NASA Langley Research Center - Atmospheric Sciences DataCenter. We are also grateful to our colleagues from the EMAC community and all other MESSy developers and users for their support. We thank A. Schmidt for editing our paper and providing the data of her paper for comparisons of our results. We would also like to thank the referees for their comments to help us improving our paper.

Appendix A: List of MESSy submodels used in this study

520 The computations for this study were performed on the Mistral supercomputer at the Deutsches Klimarechenzentrum (DKRZ), Hamburg, Germany. For this purpose, EMAC (ECHAM5/MESSy Atmospheric Chemistry), a coupled atmospheric circulation model consisting of the 5th generation of European Centre Hamburg general circulation model (ECHAM5) and the Modular Earth Submodel System (MESSy) was used.

ECHAM5 (5th generation of European Centre Hamburg general circulation model) is an atmospheric general circulation
525 model (Roeckner et al., 2003, 2006), which runs with self-consistent quasi-biennial oscillation (QBO). It is nudged to the

meteorological ERA-Interim reanalysis data of the European Centre for Medium-Range Weather Forecasts (ECMWF) up to about 100 hPa.

MESSy (Modular Earth Submodel System) is an earth system model, which consists of several submodels (Jöckel et al., 2005, 2006, 2010). An overview of the submodels used in this study is given in Table A1.

Submodel	Function	Reference
AEROPT	Aerosol optical depth	Dietmüller et al. (2016)
AIRSEA	Air-sea exchange of trace gases	Pozzer et al. (2006)
CAABA/MECCA	Atmospheric chemistry	Sander et al. (2011)
CONVECT	Convection processes	Tost et al. (2006b)
CVTRANS	Convection transport of tracers	Tost et al. (2010)
DDEP	Dry deposition	Kerkweg et al. (2006a)
GMXe	Global Modal Aerosol eXtension	Pringle et al. (2010)
IMPORT	Import of external data files	Jöckel et al. (2006)
JVAL	Photolysis rate coefficients	Jöckel et al. (2006)
LNOX	NO _x lightning production	Tost et al. (2007)
MSBM	Multiphase Stratospheric Box Model	Jöckel et al. (2010)
OFFEMIS	Off-line emissions	Kerkweg et al. (2006b)
ONEMIS	On-line emissions	Kerkweg et al. (2006b)
QBO	QBO nudging	Giorgetta et al. (2002)
RAD	RADiation	Dietmüller et al. (2016)
SCAV	Scavenging (wet removal)	Tost et al. (2006a)
SEDI	Aerosol sedimentation	Kerkweg et al. (2006a)
TNUDGE	Tracer nudging	Kerkweg et al. (2006b)
TROPOP	Tropopause calculation	Jöckel et al. (2006)

Table A1. List of used MESSy submodels. Reference and short description from <http://www.messy-interface.org>. Parts of the base model copied into MESSy which must always be active are not listed here.

530 Mineral dust emissions are calculated online using the emission scheme of Astitha et al. (2012) as part of the ONEMIS submodel. The convection was calculated with the CONVECT submodel (Tost et al., 2006b), with the convection scheme from Tiedtke (1989) and the Nordeng (1994) closure. The convection parametrization is sensitive to the model resolution, which results in differences between different model resolutions in the vertical transport of tracers, like dust, water vapor, ozone and SO₂, especially near the low latitude tropopause (Brühl et al., 2018). To avoid a phase drift, we used the QBO submodel
535 for weak nudging to the QBO zonal wind observations (Giorgetta et al., 2002). The loss of gas phase species to the aerosol is parametrized in the 3rd Equilibrium Simplified Aerosol Model (EQSAM3) (Metzger and Lelieveld, 2007). The uptake of gases on wet particles and on acid aerosol particles is included in the model calculation. Concerning removal mechanisms, the

SCAVenging submodel calculates the loss of atmospheric tracers and aerosols by wet deposition, as well as the liquid phase chemistry in clouds and precipitation (Tost et al., 2006a). The chemistry of the CAABA/MECCA submodel contains photolysis reactions, which need photolysis rate coefficients (J-values) for tropospheric and stratospheric species computed by the JVAL submodel. The RAD_FUBRAD sub-submodel is used to calculate the shortwave heating rates from the absorption of UV by O₂ and O₃ in the upper stratosphere and mesosphere.

Appendix B: Comparison of volcanic injections derived from simultaneous MIPAS, SAGE, GOMOS and OSIRIS observations

The eruption of Reventador in the tropics in November 2002 has shown to be an ideal case where simultaneous observations of all satellite sensors were available so that the direct SO₂ observation could be used for development and validation of a conversion formula for the 750 nm extinction seen by GOMOS and OSIRIS, which works also approximately for SAGE if its observations at 530 and 1025 nm are interpolated to 750 nm. Here we first use the ratio between model calculated sulfate volume mixing ratio and its share on extinction in low latitudes of the lower stratosphere which is typically $1.2 \times 10^{12} \times$ air density (in molecules/cm³). This works for medium size eruptions and data available over about four weeks following the eruptions, and if no other events occur less than about four weeks before which is the case for the Reventador eruption. If the time lag of data is several weeks a correction factor >1 has to be applied to account for removal processes, if another event is relatively close in time, the factor has to be <1 to remove the influence of the previous event. For Reventador the factor is 1 (for OSIRIS 0.8 is slightly better). For all instruments the derived injected SO₂ mass is very close to 77 kt as shown in Table 2. The spatial patterns are similar, except when the zonal wind causes a shift in longitude due to the time lag from conversion of SO₂ to aerosol, see Figure B1. In the case of SAGE, the alternate method of Grainger et al. (1995) involving aerosol surface area density (SAD) and aerosol volume density is more suitable to remove cloud perturbation. It is assumed that sulfate mixing ratios correspond to the SO₂ injected. Some uncertainty remains from removing the background which we have done by subtracting a fraction of the derived SO₂ at the longitude where it has a minimum, i.e. the longitude where the effect of the volcano is smallest for all altitudes. Integrated injected SO₂ masses for all examples are provided in Table B1.

Eruption	MIPAS	GOMOS	filled	OSIRIS	SAGE II
Reventador 2002	77	75	-	89	80
Merapi 2010	97	18	77	170	-
Sarychev 2009	446	141	-	353	-
Manda Hararo 2009	82	81	-	101	-

Table B1. Integrated mass of injected SO₂ in kt

For the eruption of Merapi in November 2010 the satellite instruments do not agree. From OSIRIS about 70% more injected SO₂ is derived than from MIPAS, i.e. 170 kt instead of 97 kt used in the transient simulation (see Table 2 and differences in

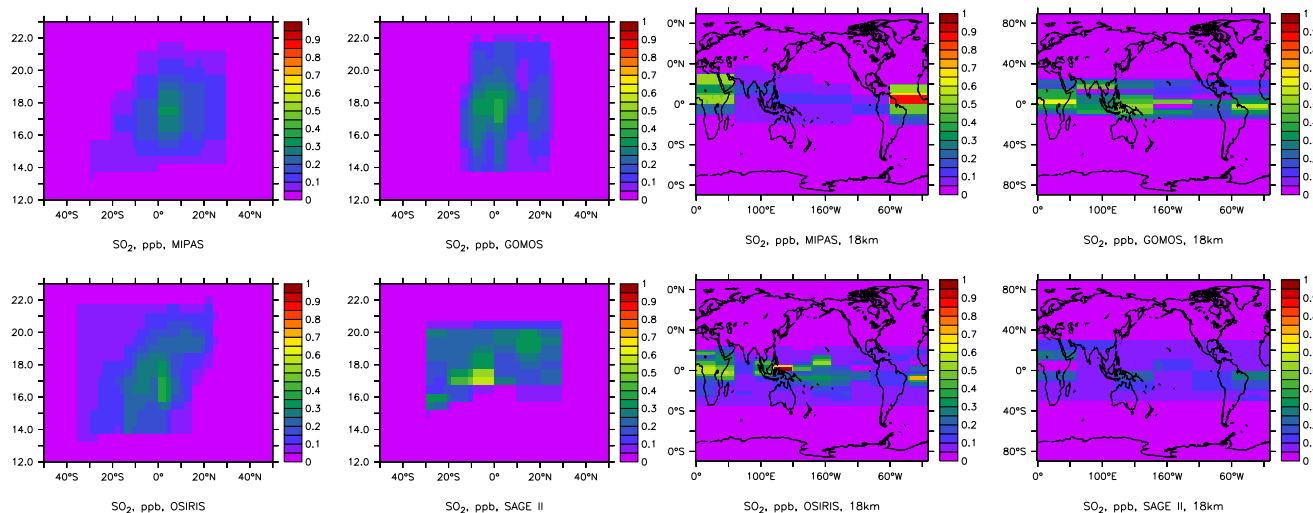


Figure B1. 2002 Reventador eruption: SO₂ derived from MIPAS and the other 3 instruments. Average vertical distribution (left) and plumes at 18 km (right). OSIRIS with correction factor 0.8 due to remnants from the Ruang eruption, SAGE II with the Grainger-based method.

Figure 10). GOMOS has too sparse data here to obtain a proper integral directly but patterns are similar (Figure B2). If other information is available, the gaps can be filled with likely values in the region where the plume was seen, a method which had to be applied also to some events seen by OSIRIS in 2018 and 2019 for which the data were sparse.

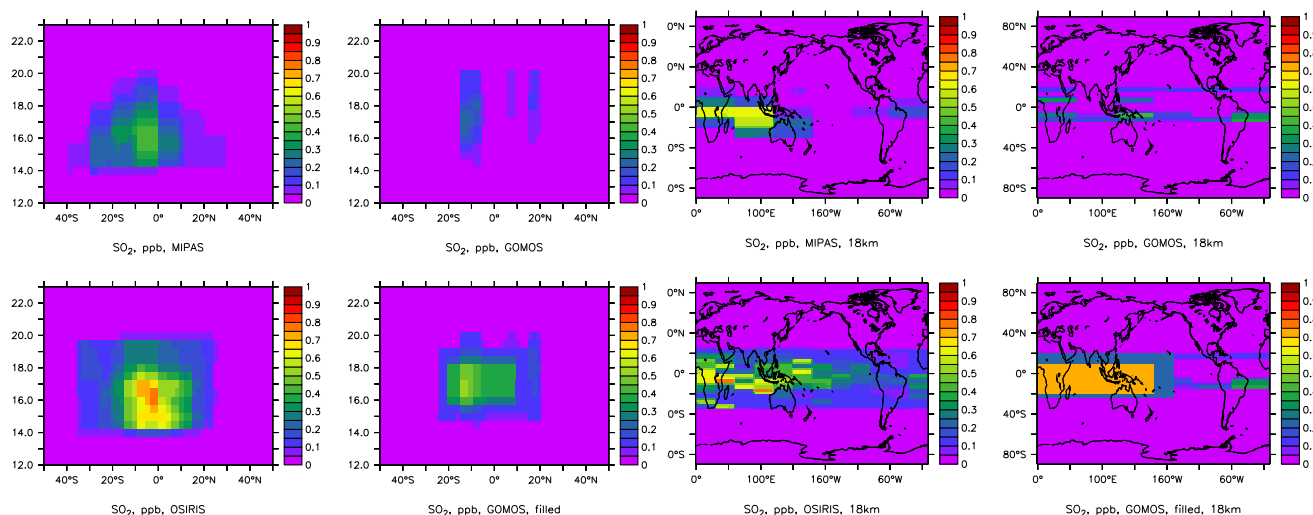


Figure B2. 2010 Merapi eruption: SO₂ derived from MIPAS, GOMOS OSIRIS and GOMOS with gap filling. Average vertical distribution (left) and plumes at 18 km (right).

For high latitude eruptions the longer conversion time of SO_2 to sulfate compared to the tropics has to be considered which, together with aerosol removal processes, lead to a weaker extinction signal. To account for this a correction factor of about two in the conversion formula for OSIRIS for example for Sarychev in June 2009 leads to values consistent to the ones derived by MIPAS (Figure B3). For the low latitude eruption of Mando Hararo in the same entry of Table 2 (separated at 24° N for the integration) the factor 1 is still appropriate.

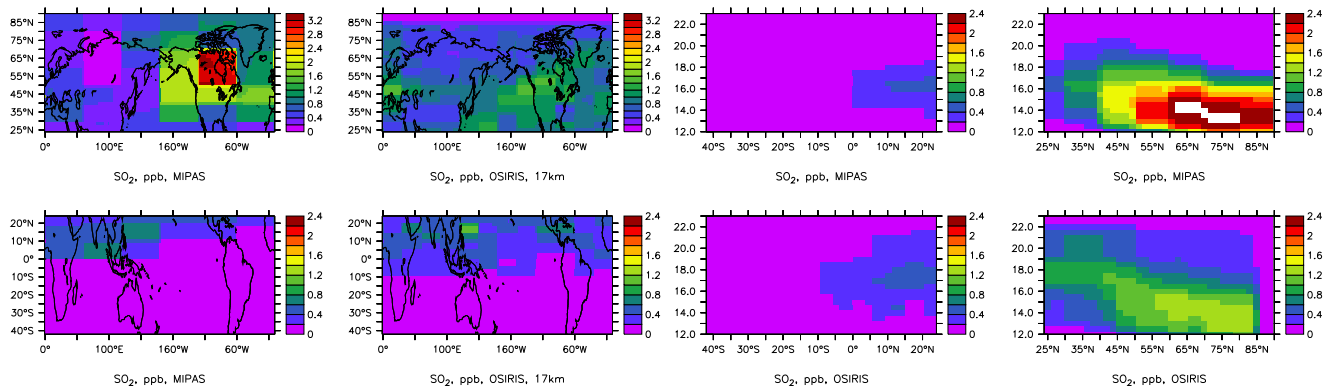


Figure B3. Sarychev and Mando Hararo from MIPAS and OSIRIS, arrangement of panels because event is split at 24° N.

Appendix C: Comparison of different volcanic injection inventories

Year	Carn et al. (2016): total SO ₂ (kt)	Carn et al. (2016): explosive SO ₂ (kt)	in %	This study: stratospheric SO ₂ (kt)
1990	186	186	100	744
1991	26082	24214	93	18424
1992	810	810	100	794
1993	450	450	100	426
1994	1874	360	19	337
1995	TOMS data gap	-	-	156
1996	987	100	10	436
1997	41	41	100	254
1998	3265	38	1.2	255
1999	130	85	65	398
2000	653	336	51	185
2001	1783	122	6.8	400
2002	2626	271	10	368
2003	679	679	100	207
2004	2997	410	14	256
2005	4634	2501	54	445
2006	1347	661	49	611
2007	712	122	17	450
2008	2625	2318	88	688
2009	1934	1379	71	839
2010	1470	867	59	424
2011	6030	4310	71	689
2012	763	563	74	355
2013	185	180	97	448
2014	5296	608	11	716
2015	-	-	-	993
2016	-	-	-	748
2017	-	-	-	600
2018	-	-	-	881
2019	-	-	-	1149

Table C1. Comparison of different volcanic emission inventories: Explosive and total annual amount of global volcanic SO₂ emissions and the percentage of explosive emissions, calculated from satellite observations in 1979 to 2014 (Carn et al., 2016), and the explosive volcanic SO₂ emissions reaching the stratosphere from the Volcanic Sulfur Emission Inventory (Table 2) in this study, ending in August 2019.

References

- Andersson, S. M., Martinsson, B. G., Vernier, J.-P., Friberg, J., Brenninkmeijer, C. a. M., Hermann, M., van Velthoven, P. F. J., and Zahn, A.: Significant radiative impact of volcanic aerosol in the lowermost stratosphere, *Nature Communications*, 6, 7692, <https://doi.org/10.1038/ncomms8692>, 2015.
- 575 Astitha, M., Lelieveld, J., Abdel Kader, M., Pozzer, A., and De Meij, A.: Parameterization of dust emissions in the global atmospheric chemistry-climate model EMAC: Impact of nudging and soil properties, *Atmospheric Chemistry and Physics*, 12, 11 057–11 083, <https://doi.org/10.5194/acp-12-11057-2012>, 2012.
- Aubry, T. J., Staunton-Sykes, J., Marshall, L. R., Haywood, J., Abraham, N. L., and Schmidt, A.: Climate change modulates the stratospheric volcanic sulfate aerosol lifecycle and radiative forcing from tropical eruptions, *Nature Communications*, 12, 1–16, <https://doi.org/10.1038/s41467-021-24943-7>, 2021.
- 580 Bertaux, J. L., Kyrölä, E., Fussen, D., Hauchecorne, A., Dalaudier, F., Sofieva, V., Tamminen, J., Vanhellemont, F., Fanton d’Andon, O., Barrot, G., Mangin, A., Blanot, L., Lebrun, J. C., Pérot, K., Fehr, T., Saavedra, L., Leppelmeier, G. W., and Fraisse, R.: Global ozone monitoring by occultation of stars: an overview of GOMOS measurements on ENVISAT, *Atmospheric Chemistry and Physics*, 10, 12 091–12 148, <https://doi.org/10.5194/acp-10-12091-2010>, 2010.
- 585 Bingen, C., Robert, C. E., Stebel, K., Brühl, C., Schallock, J., Vanhellemont, F., Mateshvili, N., Höpfner, M., Trickl, T., Barnes, J. E., Jumelet, J., Vernier, J.-P., Popp, T., de Leeuw, G., and Pinnock, S.: Stratospheric aerosol data records for the climate change initiative: Development, validation and application to chemistry-climate modelling, *Remote Sensing of Environment*, 203, 296–321, <https://doi.org/10.1016/j.rse.2017.06.002>, 2017.
- 590 Bingen, C., Robert, C., Hermans, C., Vanhellemont, F., Mateshvili, N., Dekemper, E., and Fussen, D.: A Revised Cross-Section Database for Gas Retrieval in the UV-Visible-Near IR Range, Applied to the GOMOS Retrieval Algorithm AerGOM, *Frontiers in Environmental Science*, 7, 1–18, <https://doi.org/10.3389/fenvs.2019.00118>, 2019.
- Boucher, O.: *Atmospheric Aerosols*, Springer Netherlands, Dordrecht, <https://doi.org/10.1007/978-94-017-9649-1>, 2015.
- Bourassa, A. E., Rieger, L. A., Lloyd, N. D., and Degenstein, D. A.: Odin-OSIRIS stratospheric aerosol data product and SAGE III inter-comparison, *Atmospheric Chemistry and Physics*, 12, 605–614, <https://doi.org/10.5194/acp-12-605-2012>, 2012.
- 595 Brühl, C., Lelieveld, J., Crutzen, P. J., and Tost, H.: The role of carbonyl sulphide as a source of stratospheric sulphate aerosol and its impact on climate, *Atmospheric Chemistry and Physics*, 12, 1239–1253, <https://doi.org/10.5194/acp-12-1239-2012>, 2012.
- Brühl, C., Lelieveld, J., Tost, H., Höpfner, M., and Glatthor, N.: Stratospheric sulfur and its implications for radiative forcing simulated by the chemistry climate model EMAC, *Journal of Geophysical Research*, 120, 2103–2118, <https://doi.org/10.1002/2014JD022430>, 2015.
- 600 Brühl, C., Schallock, J., Klingmüller, K., Robert, C., Bingen, C., Clarisse, L., Heckel, A., North, P., and Rieger, L.: Stratospheric aerosol radiative forcing simulated by the chemistry climate model EMAC using Aerosol CCI satellite data, *Atmospheric Chemistry and Physics*, 18, 1–15, <https://doi.org/10.5194/acp-18-12845-2018>, 2018.
- Carn, S. A., Clarisse, L., and Prata, A. J.: Multi-decadal satellite measurements of global volcanic degassing, *Journal of Volcanology and Geothermal Research*, 311, 99–134, <https://doi.org/10.1016/j.jvolgeores.2016.01.002>, 2016.
- 605 Clarisse, L., Coheur, P. F., Theys, N., Hurtmans, D., and Clerbaux, C.: The 2011 Nabro eruption, a SO₂ plume height analysis using IASI measurements, *Atmospheric Chemistry and Physics*, 14, 3095–3111, <https://doi.org/10.5194/acp-14-3095-2014>, 2014.
- Clyne, M., Lamarque, J. F., Mills, M. J., Khodri, M., Ball, W., Bekki, S., Dhomse, S. S., Lebas, N., Mann, G., Marshall, L., Niemeier, U., Poulain, V., Robock, A., Rozanov, E., Schmidt, A., Stenke, A., Sukhodolov, T., Timmreck, C., Toohey, M., Tummon, F., Zanchettin,

- D., Zhu, Y., and Toon, O. B.: Model physics and chemistry causing intermodel disagreement within the VolMIP-Tambora Interactive Stratospheric Aerosol ensemble, *Atmospheric Chemistry and Physics*, 21, 3317–3343, <https://doi.org/10.5194/acp-21-3317-2021>, 2021.
- 610 Crutzen, P. J.: The possible importance of CSO for the sulfate layer of the stratosphere, *Geophysical Research Letters*, 3, 73–76, <https://doi.org/10.1029/GL003i002p00073>, 1976.
- Dhomse, S. S., Emmerson, K. M., Mann, G. W., Bellouin, N., Carslaw, K. S., Chipperfield, M. P., Hommel, R., Abraham, N. L., Telford, P., Braesicke, P., Dalvi, M., Johnson, C. E., O'Connor, F., Morgenstern, O., Pyle, J. A., Deshler, T., Zawodny, J. M., and Thomason, L. W.: Aerosol microphysics simulations of the Mt. Pinatubo eruption with the UM-UKCA composition-climate model, *Atmospheric Chemistry and Physics*, 14, 11 221–11 246, <https://doi.org/10.5194/acp-14-11221-2014>, 2014.
- 615 Diehl, T., Heil, A., Chin, M., Pan, X., Streets, D., Schultz, M., and Kinne, S.: Anthropogenic, biomass burning, and volcanic emissions of black carbon, organic carbon, and SO₂ from 1980 to 2010 for hindcast model experiments, *Atmospheric Chemistry and Physics Discussions*, 12, 24 895–24 954, <https://doi.org/10.5194/acpd-12-24895-2012>, 2012.
- 620 Dietmüller, S., Jöckel, P., Tost, H., Kunze, M., Gellhorn, C., Brinkop, S., Frömming, C., Ponater, M., Steil, B., Lauer, A., and Hendricks, J.: A new radiation infrastructure for the Modular Earth Submodel System (MESSy, based on version 2.51), *Geoscientific Model Development*, 9, 2209–2222, <https://doi.org/10.5194/gmd-9-2209-2016>, 2016.
- English, J. M., Toon, O. B., and Mills, M. J.: Microphysical simulations of large volcanic eruptions: Pinatubo and Toba, *Journal of Geophysical Research Atmospheres*, 118, 1880–1895, <https://doi.org/10.1002/jgrd.50196>, 2013.
- 625 Fasullo, J. T., Tomas, R., Stevenson, S., Otto-Bliesner, B., Brady, E., and Wahl, E.: The amplifying influence of increased ocean stratification on a future year without a summer, *Nature Communications*, 8, 1–10, <https://doi.org/10.1038/s41467-017-01302-z>, 2017.
- Fischer, H., Birk, M., Blom, C., Carli, B., Carlotti, M., von Clarmann, T., Delbouille, L., Dudhia, A., Ehhalt, D., Endemann, M., Flaud, J. M., Gessner, R., Kleinert, A., Koopman, R., Langen, J., López-Puertas, M., Mosner, P., Nett, H., Oelhaf, H., Perron, G., Remedios, J., Ridolfi, M., Stiller, G., and Zander, R.: MIPAS: an instrument for atmospheric and climate research, *Atmospheric Chemistry and Physics*, 8, 2151–2188, <https://doi.org/10.5194/acp-8-2151-2008>, 2008.
- 630 Friberg, J., Martinsson, B. G., Andersson, S. M., and Sandvik, O. S.: Volcanic impact on the climate - The stratospheric aerosol load in the period 2006-2015, *Atmospheric Chemistry and Physics*, 18, 11 149–11 169, <https://doi.org/10.5194/acp-18-11149-2018>, 2018.
- Fromm, M., Peterson, D., and Di Girolamo, L.: The Primary Convective Pathway for Observed Wildfire Emissions in the Upper Troposphere and Lower Stratosphere: A Targeted Reinterpretation, *Journal of Geophysical Research: Atmospheres*, 124, 13 254–13 272, <https://doi.org/10.1029/2019JD031006>, 2019.
- 635 Giorgetta, M. A., Manzini, E., and Roeckner, E.: Forcing of the quasi-biennial oscillation from a broad spectrum of atmospheric waves, *Geophysical Research Letters*, 29, 86–1–86–4, <https://doi.org/10.1029/2002GL014756>, 2002.
- Giorgetta, M. A., Manzini, E., Roeckner, E., Esch, M., and Bengtsson, L.: Climatology and forcing of the quasi-biennial oscillation in the MAECHAM5 model, *Journal of Climate*, 19, 3882–3901, <https://doi.org/10.1175/JCLI3830.1>, 2006.
- 640 Glantz, P., Bourassa, A., Herber, A., Iversen, T., Karlsson, J., and Kirkevåg, A.: Remote sensing of aerosols in the Arctic for an evaluation of global climate model simulations, *Journal of Geophysical Research: Atmospheres*, 119, 8169–8188, <https://doi.org/10.1002/2013JD021279>.Received, 2014.
- Glatthor, N., Höpfner, M., Baker, I. T., Berry, J., Campbell, J. E., Kawa, S. R., Krysztofiak, G., Leyser, A., Sinnhuber, B.-M., Stiller, G. P., Stinecipher, J., and Von Clarmann, T.: Tropical sources and sinks of carbonyl sulfide observed from space, *Geophysical Research Letters*, 42, 10,082–10,090, <https://doi.org/10.1002/2015GL066293>, 2015.
- 645

- Glatthor, N., Höpfner, M., Leyser, A., Stiller, G. P., Von Clarmann, T., Grabowski, U., Kellmann, S., Linden, A., Sinnhuber, B. M., Krysztofiak, G., and Walker, K. A.: Global carbonyl sulfide (OCS) measured by MIPAS/Envisat during 2002–2012, *Atmospheric Chemistry and Physics*, 17, 2631–2652, <https://doi.org/10.5194/acp-17-2631-2017>, 2017.
- Grainger, R. G., Lambert, A., Rodgers, C. D., Taylor, F. W., and Deshler, T.: Stratospheric aerosol effective radius, surface area and volume estimated from infrared measurements, *Journal of Geophysical Research*, 100, 16 507–16 518, <https://doi.org/10.1029/95JD00988>, 1995.
- 650 Guo, S., Bluth, G. J., Rose, W. I., Watson, I. M., and Prata, A. J.: Re-evaluation of SO₂ release of the 15 June 1991 Pinatubo eruption using ultraviolet and infrared satellite sensors, *Geochemistry, Geophysics, Geosystems*, 5, 1–31, <https://doi.org/10.1029/2003GC000654>, 2004.
- Höpfner, M., Glatthor, N., Grabowski, U., Kellmann, S., Kiefer, M., Linden, A., Orphal, J., Stiller, G. P., von Clarmann, T., Funke, B., and Boone, C. D.: Sulfur dioxide (SO₂) as observed by MIPAS/Envisat: temporal development and spatial distribution at 15–45km altitude, *Atmospheric Chemistry and Physics*, 13, 10 405–10 423, <https://doi.org/10.5194/acp-13-10405-2013>, 2013.
- 655 Höpfner, M., Boone, C. D., Funke, B., Glatthor, N., Grabowski, U., Günther, A., Kellmann, S., Kiefer, M., Linden, A., Lossow, S., Pumphrey, H. C., Read, W. G., Roiger, A., Stiller, G. P., Schlager, H., Von Clarmann, T., and Wissmüller, K.: Sulfur dioxide (SO₂) from MIPAS in the upper troposphere and lower stratosphere 2002–2012, *Atmospheric Chemistry and Physics*, 15, 7017–7037, <https://doi.org/10.5194/acp-15-7017-2015>, 2015.
- 660 IPCC: 2013: Climate Change 2013: The Physical Science Basis. Contribution of Working Group I to the Fifth Assessment Report of the Intergovernmental Panel on Climate Change, Cambridge University Press, Cambridge, United Kingdom and New York, NY, USA, <https://doi.org/10.1017/CBO9781107415324>, 2013.
- Jöckel, P., Sander, R., Kerkweg, A., Tost, H., and Lelieveld, J.: Technical Note: The Modular Earth Submodel System (MESSy) – a new approach towards Earth System Modeling, *Atmospheric Chemistry and Physics*, 4, 7139–7166, <https://doi.org/10.5194/acpd-4-7139-2004>, 2005.
- 665 Jöckel, P., Tost, H., Pozzer, A., Brühl, C., Buchholz, J., Ganzeveld, L., Hoor, P., Kerkweg, A., Lawrence, M. G., Sander, R., Steil, B., Stiller, G., Tanarhte, M., Taraborrelli, D., van Aardenne, J., and Lelieveld, J.: The atmospheric chemistry general circulation model ECHAM5/MESSy1: consistent simulation of ozone from the surface to the mesosphere, *Atmospheric Chemistry and Physics*, 6, 6957–7050, <https://doi.org/10.5194/acpd-6-6957-2006>, 2006.
- 670 Jöckel, P., Kerkweg, A., Pozzer, A., Sander, R., Tost, H., Riede, H., Baumgaertner, A., Gromov, S., and Kern, B.: Development cycle 2 of the Modular Earth Submodel System (MESSy2), *Geoscientific Model Development*, 3, 717–752, <https://doi.org/10.5194/gmd-3-717-2010>, 2010.
- Kerkweg, A.: Global Modelling of Atmospheric Halogen Chemistry in the Marine Boundary Layer, Ph.D. thesis, Friedrich-Wilhelms-Universität Bonn, 2005.
- 675 Kerkweg, A., Buchholz, J., Ganzeveld, L., Pozzer, A., Tost, H., and Jöckel, P.: Technical Note: An implementation of the dry removal processes DRY DEPosition and SEDimentation in the Modular Earth Submodel System (MESSy), *Atmospheric Chemistry and Physics*, 6, 6853–6901, <https://doi.org/10.5194/acpd-6-6853-2006>, 2006a.
- Kerkweg, A., Sander, R., Tost, H., and Jöckel, P.: Technical Note: Implementation of prescribed (OFFLEM), calculated (ONLEM), and pseudo-emissions (TNUDGE) of chemical species in the Modular Earth Submodel System (MESSy), *Atmospheric Chemistry and Physics*, 6, 5485–5504, <https://doi.org/10.5194/acpd-6-5485-2006>, 2006b.
- 680 Kettle, A. J. and Andreae, M. O.: Flux of dimethylsulfide from the oceans: A comparison of updated data sets and flux models, *Journal of Geophysical Research*, 105, 26 793–26 808, <https://doi.org/10.1029/2000JD900252>, 2000.

- Klingmüller, K., Metzger, S., Abdelkader, M., Karydis, V. A., Stenchikov, G. L., Pozzer, A., and Lelieveld, J.: Revised mineral dust emissions in the atmospheric chemistry–climate model EMAC (MESSy 2.52 DU_Astitha1 KKDU2017 patch), *Geoscientific Model Development*, 11, 989–1008, <https://doi.org/10.5194/gmd-11-989-2018>, 2018.
- 685 Kloss, C., Berthet, G., Sellitto, P., Ploeger, F., Bucci, S., Khaykin, S., Jégou, F., Taha, G., Thomason, L. W., Barret, B., Le Flochmoen, E., Von Hobe, M., Bossolasco, A., Bègue, N., and Legras, B.: Transport of the 2017 canadian wildfire plume to the tropics via the asian monsoon circulation, *Atmospheric Chemistry and Physics*, 19, 13 547–13 567, <https://doi.org/10.5194/acp-19-13547-2019>, 2019.
- Kloss, C., Berthet, G., Sellitto, P., Ploeger, F., Taha, G., Tidiga, M., Eremenko, M., Bossolasco, A., Jégou, F., Renard, J. B., and Legras, B.: Stratospheric aerosol layer perturbation caused by the 2019 Raikoke and Ulawun eruptions and their radiative forcing, *Atmospheric Chemistry and Physics*, 21, 535–560, <https://doi.org/10.5194/acp-21-535-2021>, 2021.
- 690 Kovilakam, M., W. Thomason, L., Ernest, N., Rieger, L., Bourassa, A., and Millan, L.: The Global Space-based Stratospheric Aerosol Climatology (version 2.0): 1979–2018, *Earth System Science Data*, 12, 2607–2634, <https://doi.org/10.5194/essd-12-2607-2020>, 2020.
- Kyrölä, E., Tamminen, J., Sofieva, V., Bertaux, J. L., Hauchecorne, A., Dalaudier, F., Fussen, D., Vanhellemont, F., Fanton D’Andon, O., Barrot, G., Guirlet, M., Fehr, T., and Saavedra De Miguel, L.: GOMOS O₃, NO₂, and NO₃ observations in 2002–2008, *Atmospheric Chemistry and Physics*, 10, 7723–7738, <https://doi.org/10.5194/acp-10-7723-2010>, 2010.
- 695 Long, C. S. and Stowe, L. L.: using the NOAA/AVHRR to study stratospheric aerosol optical thicknesses following the Mt. Pinatubo Eruption, *Geophysical Research Letters*, 21, 2215–2218, <https://doi.org/10.1029/94GL01322>, 1994.
- McGregor, H. V., Evans, M. N., Goosse, H., Leduc, G., Martrat, B., Addison, J. A., Mortyn, P. G., Oppo, D. W., Seidenkrantz, M. S., Sicre, M. A., Phipps, S. J., Selvaraj, K., Thirumalai, K., Filipsson, H. L., and Ersek, V.: Robust global ocean cooling trend for the pre-industrial Common Era, *Nature Geoscience*, 8, 671–677, <https://doi.org/10.1038/ngeo2510>, 2015.
- 700 Metzger, S. and Lelieveld, J.: Reformulating atmospheric aerosol thermodynamics and hygroscopic growth into haze and clouds, *Atmospheric Chemistry and Physics*, 7, 849–910, <https://doi.org/10.5194/acpd-7-849-2007>, 2007.
- Mills, M. J., Schmidt, A., Easter, R., Solomon, S., Kinnison, D. E., Ghan, S. J., Neely, R. R., Marsh, D. R., Conley, A., Bardeen, C. G., and Gettelman, A.: Global volcanic aerosol properties derived from emissions, 1990–2014, using CESM1(WACCM), *Journal of Geophysical Research*, 121, 2332–2348, <https://doi.org/10.1002/2015JD024290>, 2016.
- 705 Minnis, P., Harrison, E. F., Stowe, L. L., Gibson, G. G., Denn, F. M., Doelling, D. R., and Smith, W. L.: Radiative climate forcing by the Mount Pinatubo eruption, *Science*, 259, 1411–1415, <https://doi.org/10.1126/science.259.5100.1411>, 1993.
- Nordeng, T. E.: Extended version of the convective parametrization scheme at ECMWF and their impact on the mean and transient activity of the model in the tropics, Tech. rep., ECMWF, 1994.
- 710 Pozzer, A., Jöckel, P., Sander, R., Williams, J., Ganzeveld, L., and Lelieveld, J.: Technical Note: The MESSy-submodel AIRSEA calculating the air-sea exchange of chemical species, *Atmospheric Chemistry and Physics*, 6, 5435–5444, <https://doi.org/10.5194/acp-6-5435-2006>, 2006.
- Pringle, K. J., Tost, H., Metzger, S., Steil, B., Giannadaki, D., Nenes, A., Fountoukis, C., Stier, P., Vignati, E., and Lelieveld, J.: Description and evaluation of GMXe: a new aerosol submodel for global simulations (v1), *Geoscientific Model Development*, 3, 391–412, <https://doi.org/10.5194/gmd-3-391-2010>, 2010.
- 715 Rieger, L. A., Bourassa, A. E., and Degenstein, D. A.: Merging the OSIRIS and SAGE II stratospheric aerosol records, *Journal of Geophysical Research*, 120, 8890–8904, <https://doi.org/10.1002/2015JD023133>, 2015.

- Rieger, L. A., Malinina, E. P., Rozanov, A. V., Burrows, J. P., Bourassa, A. E., and Degenstein, D. A.: A study of the approaches used to retrieve aerosol extinction, as applied to limb observations made by OSIRIS and SCIAMACHY, *Atmospheric Measurement Techniques*, 11, 3433–3445, <https://doi.org/10.5194/amt-11-3433-2018>, 2018.
- Rieger, L. A., Zawada, D. J., Bourassa, A. E., and Degenstein, D. A.: A Multiwavelength Retrieval Approach for Improved OSIRIS Aerosol Extinction Retrievals, *Journal of Geophysical Research: Atmospheres*, 124, 2018JD029897, <https://doi.org/10.1029/2018JD029897>, 2019.
- Rieger, L. A., Cole, J. N., Fyfe, J. C., Po-Chedley, S., Cameron-Smith, P. J., Durack, P. J., Gillett, N. P., and Tang, Q.: Quantifying CanESM5 and EAMv1 sensitivities to Mt. Pinatubo volcanic forcing for the CMIP6 historical experiment, *Geoscientific Model Development*, 13, 4831–4843, <https://doi.org/10.5194/gmd-13-4831-2020>, 2020.
- Rinsland, C. P., Gunson, M. R., Ko, M. K., Weisenstein, D. W., Zander, R., Abrams, M. C., Goldman, A., Sze, N. D., and Yue, G. K.: H₂SO₄ photolysis: A source of sulfur dioxide in the upper stratosphere, *Geophysical Research Letters*, 22, 1109–1112, <https://doi.org/10.1029/95GL00917>, 1995.
- Robert, C. É., Bingen, C., Vanhellemont, F., Mateshvili, N., Dekemper, E., Tétard, C., Fussen, D., Bourassa, A., and Zehner, C.: AerGOM, an improved algorithm for stratospheric aerosol retrieval from GOMOS observations. Part 2: Intercomparisons, *Atmospheric Measurement Techniques*, 9, 4701–4718, <https://doi.org/10.5194/amt-9-4701-2016>, 2016.
- Roeckner, E., Bäuml, G., Bonaventura, L., Brokopf, R., Esch, M., Giorgetta, M., Hagemann, S., Kirchner, I., Kornbluh, L., Manzini, E., Rhodin, A., Schlese, U., Schulzweida, U., and Tompkins, A.: The atmospheric general circulation model ECHAM5. Part I: Model description., Tech. Rep. 349, Max-Planck-Institute für Meteorologie, Hamburg, <https://doi.org/10.1029/2010JD014036>, 2003.
- Roeckner, E., Brokopf, R., Esch, M., Giorgetta, M. A., Hagemann, S., Kornbluh, L., Manzini, E., Schlese, U., and Schulzweida, U.: Sensitivity of simulated climate to horizontal and vertical resolution in the ECHAM5 atmosphere model, *Journal of Climate*, 19, 3771–3791, <https://doi.org/10.1175/JCLI3824.1>, 2006.
- Sander, R., Baumgaertner, A., Gromov, S., Harder, H., Jöckel, P., Kerkweg, A., Kubistin, D., Regelin, E., Riede, H., Sandu, A., Taraborrelli, D., Tost, H., and Xie, Z.-Q. Q.: The atmospheric chemistry box model CAABA/MECCA-3.0, *Geoscientific Model Development*, 4, 373–380, <https://doi.org/10.5194/gmd-4-373-2011>, 2011.
- Santer, B. D., Bonfils, C., Painter, J. F., Zelinka, M. D., Mears, C., Solomon, S., Schmidt, G. A., Fyfe, J. C., Cole, J. N., Nazarenko, L., Taylor, K. E., and Wentz, F. J.: Volcanic contribution to decadal changes in tropospheric temperature, *Nature Geoscience*, 7, 185–189, <https://doi.org/10.1038/ngeo2098>, 2014.
- Schmidt, A., Mills, M. J., Ghan, S., Gregory, J. M., Allan, R. P., Andrews, T., Bardeen, C. G., Conley, A., Forster, P. M., Gettelman, A., Portmann, R. W., Solomon, S., and Toon, O. B.: Volcanic Radiative Forcing From 1979 to 2015, *Journal of Geophysical Research: Atmospheres*, 123, 12,491–12,508, <https://doi.org/10.1029/2018JD028776>, 2018.
- Solomon, S., Daniel, J. S., Neely, R. R., Vernier, J.-P., Dutton, E. G., and Thomason, L. W.: The persistently variable "background" stratospheric aerosol layer and global climate change, *Science*, 333, 866–870, <https://doi.org/10.1126/science.1206027>, 2011.
- Stier, P., Feichter, J., Kinne, S., Kloster, S., Vignati, E., Wilson, J., Ganzeveld, L., Tegen, I., and Werner, M.: The aerosol-climate model ECHAM5-HAM, *Atmospheric Chemistry and Physics*, 5, 1125–1156, 2005.
- Swindles, G. T., Savov, I. P., Schmidt, A., Hooper, A., Connor, C. B., and Carrivick, J. L.: Climatic control on Icelandic volcanic activity during the mid-Holocene: REPLY, *Geology*, 46, 47–50, <https://doi.org/10.1130/G40290Y.1>, 2018.
- Thomason, L. W., Burton, S. P., Luo, B. P., and Peter, T.: SAGE II measurements of stratospheric aerosol properties at non-volcanic levels, *Atmospheric Chemistry and Physics*, 8, 983–995, 2008.

- Thomason, L. W., Ernest, N., Millán, L., Rieger, L., Bourassa, A., Vernier, J.-P., Manney, G., Luo, B., Arfeuille, F., and Peter, T.: A global space-based stratospheric aerosol climatology: 1979–2016, *Earth System Science Data*, 10, 469–492, <https://doi.org/10.5194/essd-10-469-2018>, 2018.
- 760 Tiedtke, M.: A Comprehensive Mass Flux Scheme for Cumulus Parameterization in Large-Scale Models, *Monthly Weather Review*, 117, 1779–1800, [https://doi.org/10.1175/1520-0493\(1989\)117<1779:ACMFSF>2.0.CO;2](https://doi.org/10.1175/1520-0493(1989)117<1779:ACMFSF>2.0.CO;2), 1989.
- Timmreck, C.: Modeling the climatic effects of large explosive volcanic eruptions, *Wiley Interdisciplinary Reviews: Climate Change*, 3, 545–564, <https://doi.org/10.1002/wcc.192>, 2012.
- Timmreck, C., Graf, H. F., and Feichter, J.: Simulation of Mt. Pinatubo volcanic aerosol with the Hamburg climate model ECHAM4, *Theoretical and Applied Climatology*, 62, 85–108, <https://doi.org/10.1007/s007040050076>, 1999.
- 765 Timmreck, C., Mann, G. W., Aquila, V., Hommel, R., Lee, L. A., Schmidt, A., Brühl, C., Carn, S., Chin, M., Dhomse, S. S., Diehl, T., English, J. M., Mills, M. J., Neely, R., Sheng, J., Toohey, M., and Weisenstein, D.: The Interactive Stratospheric Aerosol Model Intercomparison Project (ISA-MIP): Motivation and experimental design, *Geoscientific Model Development*, 11, 2581–2608, <https://doi.org/10.5194/gmd-11-2581-2018>, 2018.
- 770 Toohey, M., Krüger, K., Niemeier, U., and Timmreck, C.: The influence of eruption season on the global aerosol evolution and radiative impact of tropical volcanic eruptions, *Atmospheric Chemistry and Physics*, 11, 12 351–12 367, <https://doi.org/10.5194/acp-11-12351-2011>, 2011.
- Tost, H., Jöckel, P., Kerkweg, A., Sander, R., and Lelieveld, J.: Technical note: A new comprehensive SCAVenging submodel for global atmospheric chemistry modelling, *Atmospheric Chemistry and Physics*, 5, 11 157–11 181, <https://doi.org/10.5194/acpd-5-11157-2005>, 2006a.
- 775 Tost, H., Jöckel, P., and Lelieveld, J.: Influence of different convection parameterisations in a GCM, *Atmospheric Chemistry and Physics*, 6, 5475–5493, <https://doi.org/10.5194/acp-6-5475-2006>, 2006b.
- Tost, H., Jöckel, P., and Lelieveld, J.: Lightning and convection parameterisations - uncertainties in global modelling, *Atmospheric Chemistry and Physics*, 7, 4553–4568, <https://doi.org/10.5194/acpd-7-6767-2007>, 2007.
- 780 Tost, H., Lawrence, M. G., Brühl, C., and Jöckel, P.: Uncertainties in atmospheric chemistry modelling due to convection parameterisations and subsequent scavenging, *Atmospheric Chemistry and Physics*, 10, 1931–1951, <https://doi.org/10.5194/acp-10-1931-2010>, 2010.
- Vanhellemont, F., Fussen, D., and Bingen, C.: Global one-step inversion of satellite occultation measurements: A practical method, *Journal of Geophysical Research*, 109, D09 306, <https://doi.org/10.1029/2003JD004168>, 2004.
- Vanhellemont, F., Fussen, D., Matshvili, N., Tétard, C., Bingen, C., Dekemper, E., Loodts, N., Kyrölä, E., Sofieva, V., Tamminen, J., *Hauchecorne, A., Bertaux, J. L., Dalaudier, F., Blanot, L., Fanton D’Andon, O., Barrot, G., Guirlet, M., Fehr, T., and Saavedra, L.:* Optical extinction by upper tropospheric/stratospheric aerosols and clouds: GOMOS observations for the period 2002–2008, *Atmospheric Chemistry and Physics*, 10, 7997–8009, <https://doi.org/10.5194/acp-10-7997-2010>, 2010.
- 785 Vanhellemont, F., Matshvili, N., Blanot, L., Robert, C. É., Bingen, C., Sofieva, V., Dalaudier, F., Tétard, C., Fussen, D., Dekemper, E., Kyrölä, E., Laine, M., Tamminen, J., and Zehner, C.: AerGOM, an improved algorithm for stratospheric aerosol retrieval from GOMOS observations. Part 1: Algorithm description, *Atmospheric Measurement Techniques*, 2016, 1–24, <https://doi.org/10.5194/amt-2016-27>, 2016.
- 790 Vehkamäki, H., Kulmala, M., Napari, I., Lehtinen, K. E. J., Timmreck, C., Noppel, M., and Laaksonen, A.: An improved parameterization for sulfuric acid – water nucleation rates for tropospheric and stratospheric conditions, *Journal of Geophysical Research*, 107, 1–10, <https://doi.org/10.1029/2002JD002184>, 2002.

- 795 Vernier, J.-P., Thomason, L. W., Pommereau, J.-P. P., Bourassa, A. E., Pelon, J., Garnier, A., Hauchecorne, A., Blanot, L., Trepte, C.,
Degenstein, D. A., and Vargas, F.: Major influence of tropical volcanic eruptions on the stratospheric aerosol layer during the last decade,
Geophysical Research Letters, 38, 1–8, <https://doi.org/10.1029/2011GL047563>, 2011.
- Vernier, J.-P., Fairlie, T. D., Deshler, T., Natarajan, M., Knepp, T., Foster, K., Wienhold, F. G., Bedka, K. M., Thomason, L., and Trepte, C.:
In situ and space-based observations of the Kelud volcanic plume: The persistence of ash in the lower stratosphere, Journal of Geophysical
800 Research : Atmospheres, 121, 104–118, <https://doi.org/10.1002/2016JD025344>, 2016.
- Vignati, E., Wilson, J., and Stier, P.: M7: An efficient size-resolved aerosol microphysics module for large-scale aerosol transport models,
Journal of Geophysical Research: Atmospheres, 109, <https://doi.org/10.1029/2003JD004485>, 2004.
- Wilson, J. C., Lee, S. H., Reeves, J. M., Brock, C. A., Jonsson, H. H., Lafleur, B. G., Loewenstein, M., Podolske, J., Atlas, E., Boering, K.,
Toon, G., Fahey, D., Bui, T. P., Diskin, G., and Moore, F.: Steady-state aerosol distributions in the extra-tropical, lower stratosphere and
805 the processes that maintain them, Atmospheric Chemistry and Physics, 8, 6617–6626, <https://doi.org/10.5194/acp-8-6617-2008>, 2008.
- Wong, T., Wielicki, B. A., Lee, R. B., Smith, G. L., Bush, K. A., and Willis, J. K.: Reexamination of the observed decadal variability
of the earth radiation budget using altitude-corrected ERBE/ERBS nonscanner WFOV data, Journal of Climate, 19, 4028–4048,
<https://doi.org/10.1175/JCLI3838.1>, 2006.
- Zhu, Y., Toon, O. B., Jensen, E. J., Bardeen, C. G., Mills, M. J., Tolbert, M. A., Yu, P., and Woods, S.: Persisting volcanic ash particles impact
810 stratospheric SO₂ lifetime and aerosol optical properties, Nature Communications, 11, 1–11, <https://doi.org/10.1038/s41467-020-18352-5>,
2020.